

# Diperfluorophenyl Fused Thiophene Semiconductors for n-Type Organic Thin Film Transistors (OTFTs)

Jangdae Youn, Sureshrajou Vegiraju, Jonathan D. Emery, Benjamin J. Leever, Sumit Kewalramani, Silvia J. Lou, Shiming Zhang, Kumaresan Prabakaran, Yamuna Ezhumalai, Choongik Kim,\* Peng-Yi Huang, Charlotte Stern, Wen-Chung Chang, Michael J. Bedzyk,\* Lin X. Chen,\* Ming-Chou Chen,\* Antonio Facchetti,\* and Tobin J. Marks\*

Three new fused thiophene semiconductors, end-capped with diperfluorophenylthien-2-yl (DFPT) groups (DFPT-thieno[2',3':4,5]thieno[3,2-b]thieno[2,3-d]thiophene (TTA), DFPT-dithieno[2,3-b:3',2'-d]thiophenes (DTT), and DFPT-thieno[3,2-b]thiophene (TT)), are synthesized and characterized in organic thin film transistors. Good environmental stability of the newly developed materials is demonstrated via thermal analysis as well as degradation tests under white light. The molecular structures of all three perfluorophenylthien-2-yl end-functionalized derivatives are determined by single crystal X-ray diffraction. DFPT-TTA and DFPT-TT exhibit good n-type TFT performance, with mobilities up to 0.43 and 0.33 cm<sup>2</sup> V<sup>-1</sup> s<sup>-1</sup>, respectively. These are among the best performing n-type materials of all fused thiophenes reported to date. The best thin film transistor device performance is achieved via an *n*-octadecyltrichlorosilane dielectric surface treatment on the thermally grown Si/SiO<sub>2</sub> substrates prior to vapor-phase semiconductor deposition. Within the DFPT series, carrier mobility magnitudes depend strongly on the semiconductor growth conditions and the gate dielectric surface treatment.

## 1. Introduction

Organic thin film transistors (OTFTs) have attracted great attention over the last decade as a promising solution for low-cost, large-area flexible electronics.<sup>[1–10]</sup> The growing interest in high-performance, air-stable organic semiconductors has benefited greatly from the development of fused thiophene derivatives<sup>[11–13]</sup>

as a viable alternative to acene-based small molecule materials.<sup>[14–19]</sup> Among several fused thiophene derivatives reported,<sup>[20–26]</sup> there have been a few quinoidal n-channel fused thiophenes.<sup>[21,22]</sup> Although devices based on quinoidal n-channel fused thiophene derivatives showed relatively high electrical performance, there have been a few limitations: i) synthesis of these materials is challenging, ii) large amounts of (expensive) Pd catalyst (e.g., 0.3–1.0 eq.) are required for the synthesis of these materials,<sup>[21a,21b]</sup> and iii) synthetic yields of these materials are relatively low (usually 20–40%). To this end, alternative strategies to promote electron transport in such systems are required to functionalize fused thiophene-based semiconductors with strong electron-withdrawing substituents, such as the perfluoroaryl<sup>[25]</sup> and carbonyl<sup>[27]</sup> groups. Previously, we explored the charge transport properties of dithieno[2,3-b:3',2'-d]thiophenes (DTT) having three fused thiophene units with perfluorophenyl or perfluorobenzoyl substitution (**Figure 1**).<sup>[26]</sup> These three DTTs—DFP-DTT, FBB-DTT, and DFB-DTT—fabricated as vapor-deposited films, exhibit electron mobilities of 0.07, 0.03, and 0.003 cm<sup>2</sup> V<sup>-1</sup> s<sup>-1</sup>, respectively. Since additional fused thiophenes should further extend the  $\pi$ -conjugation, we extended this strategy by functionalizing

Dr. J. Youn, S. J. Lou, Dr. S. Zhang, Dr. C. Stern, Prof. L. X. Chen, Prof. A. Facchetti, Prof. T. J. Marks  
Department of Chemistry and the Materials Research Center  
Northwestern University  
2145 Sheridan Road, Evanston, IL 60208-3113, USA  
E-mail: l-chen@northwestern.edu; a-facchetti@northwestern.edu; t-marks@northwestern.edu

S. Vegiraju, Dr. K. Prabakaran, Dr. Y. Ezhumalai,  
Dr. P.-Y. Huang, Dr. W.-C. Chang, Prof. M.-C. Chen  
Department of Chemistry  
National Central University  
Jhong-Li 320, Taiwan  
E-mail: mcchen@ncu.edu.tw

DOI: 10.1002/aelm.201500098

Dr. J. D. Emery, Dr. B. J. Leever, Dr. S. Kewalramani,  
Prof. M. J. Bedzyk  
Department of Materials Science and Engineering  
Northwestern University  
2145 Sheridan Road, Evanston, IL 60208-3113, USA  
E-mail: bedzyk@northwestern.edu

Dr. B. J. Leever  
Air Force Research Laboratory  
2941 Hobson Way, Wright-Patterson AFB, OH 45433-7750, USA  
Prof. C. Kim  
Department of Chemical and Biomolecular Engineering  
Sogang University  
1 Shinsoo-dong, Mapo-gu, Seoul 121742, Korea  
E-mail: choongik@sogang.ac.kr



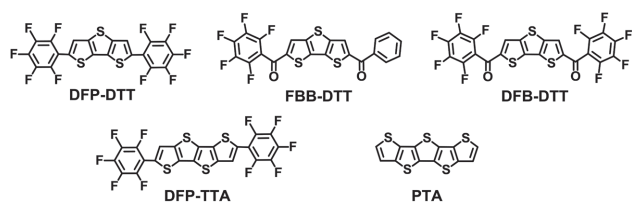


**Figure 1.** Examples of n-channel organic semiconductors based on fused thiophenes–dithienothiophenes (DTTs), tetrathienoacene (TTA), and pentathienoacene (PTA).

fused four-thiophene structures, tetrathienoacenes (TTA), with perfluorophenyl groups and found n-type mobilities as high as  $0.30 \text{ cm}^2 \text{ V}^{-1} \text{ s}^{-1}$  (DFP-TTA).<sup>[28]</sup>

To further enhance OTFT performance, we envisioned extending the fused thiophene  $\pi$ -conjugation by increasing the number of fused thiophene ring cores from tetrathienoacene to pentathienoacene (PTA).<sup>[24b]</sup> However, owing to the low solubility of PTA, further functionalization of PTA is not effective. Besides, PTA is more difficult to obtain, with much lower synthetic yield (<10%), compared to TTA. However, the insertion of additional thiophene rings into the DFP-TTA skeleton may achieve this purpose. Here we implement the following approach: a four fused thiophene TTA core is end-functionalized with a perfluorophenylthien-2-yl (FPT) group to yield diperfluorophenylthien-2-yl (DFPT)-TTA (**Figure 2**). The resultant film exhibits high n-type charge transport with a mobility up to  $\mu = 0.43 \text{ cm}^2 \text{ V}^{-1} \text{ s}^{-1}$ , an  $\approx 40\%$  increase over DFP-TTA. For comparison, two other FPT-functionalized fused thiophenes, DFPT-DTT and DFPT-thieno[3,2-*b*]thiophene (TT), are also prepared (**Figure 2**). Of these, DFPT-TT exhibits n-channel carrier mobility with  $\mu$  as high as  $0.33 \text{ cm}^2 \text{ V}^{-1} \text{ s}^{-1}$ , a 10% increase over DFP-TTA. The materials properties of these newly synthesized DFPTs, such as the crystal structures, HOMO–LUMO energetics, and film microstructure, are discussed and compared to the DFP analogs. In addition, film growth conditions, such as substrate temperature and dielectric surface treatment, are investigated and shown to strongly influence thin film transistor device response.

## 2. Results and Discussion

### 2.1. Synthesis

As shown in **Figure 3**, the synthesis of DFPT-end-capped fused thiophenes is achieved via Stille coupling. First, deprotonation

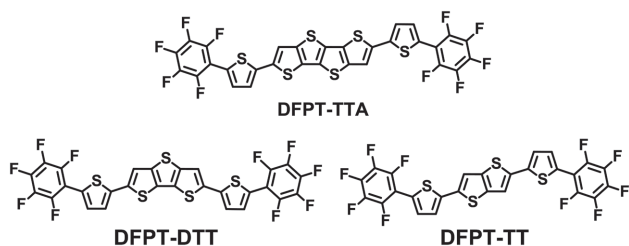


**Figure 2.** The diperfluorophenylthien-2-yl (DFPT)-functionalized fused thiophene organic semiconductors synthesized and characterized in this study.

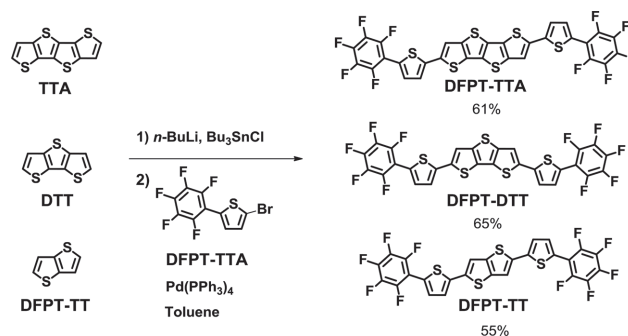


**Figure 3.** The synthesis of DFPT derivatives employed in this study.

of the fused thiophene (TTA, DTT, or TT) is followed by aryl stannylation, with the corresponding fused thiophene–SnR<sub>3</sub> derivatives generated in situ. Next, through the double coupling of the above stannylated fused thiophenes with the aryl bromide FPT-Br, the corresponding final products, DFPT-TTA, DFPT-DTT, and DFPT-TT, are produced in an  $\approx 60\%$  yield. All three compounds were characterized by conventional chemical and physical methods, and their molecular structures were confirmed by single crystal X-ray diffraction.

### 2.2. Semiconductor Optical and Thermal Properties

The optical absorption spectra of the DFPT-end-capped molecules in *o*-C<sub>6</sub>H<sub>4</sub>Cl<sub>2</sub> solution are significantly red-shifted versus their DFP-end-capped analogs, as shown in **Figure 4**. For the DFPT derivatives, the four fused thiophene–TTA system ( $\lambda_{\text{max}} \approx 438 \text{ nm}$ ) has a greater  $\pi$ -electron delocalization than in the DTT system ( $\lambda_{\text{max}} \approx 432 \text{ nm}$ ), affording the lowest energy gap for the organic semiconductors synthesized in this study (**Table 1**).

Note that DFPT-TT absorption is red-shifted ( $\lambda_{\text{max}} \approx 418 \text{ nm}$ ) compared to that of DFP-TTA ( $\lambda_{\text{max}} \approx 385 \text{ nm}$ ), due to the greater  $\pi$ -electron expanse. The HOMO–LUMO energy gaps

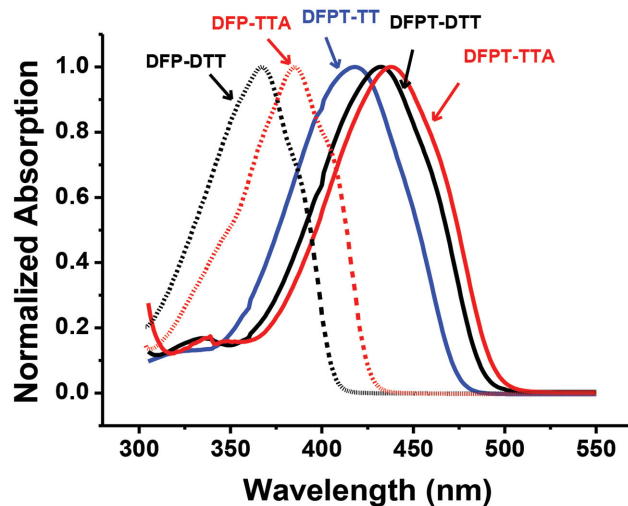


**Figure 4.** Optical absorption spectra of DFPT- and DFP-end-capped organic semiconductors in *o*-C<sub>6</sub>H<sub>4</sub>Cl<sub>2</sub> solution.

**Table 1.** Comparison of the thermal, optical, and electrochemical properties of DFPT- and DFP-end-capped semiconductors.

Compound	DSC $T_m$ (°C)	TGA (°C; 5%)	UV-vis <sup>a)</sup> $\lambda_{max}$ (nm)	Potential <sup>b)</sup> [V]		$E_{gap}$ [eV]	
				$E_{red}$	$E_{ox}$	UV <sup>a)</sup>	DPV <sup>b)</sup>
DFPT-TTA	329	401	438	-1.63	1.14	2.51	2.77
DFPT-DTT	319	369	432	-1.63	1.22	2.55	2.86
DFPT-TT	239	319	418	-1.65	1.29	2.62	2.94
DFP-TTA	>280	330	385	-1.66 <sup>c)</sup>	1.46 <sup>c)</sup>	2.93	3.12
DFP-DTT	258	270	367	-1.62 <sup>c)</sup>	1.64 <sup>c)</sup>	3.06	3.26
Pentacene <sup>d)</sup>	373	297	579	-1.27	0.80	2.07	2.09

<sup>a)</sup>In *o*-C<sub>6</sub>H<sub>4</sub>Cl<sub>2</sub> at 25 °C; <sup>b)</sup>By DPV in *o*-C<sub>6</sub>H<sub>4</sub>Cl<sub>2</sub> at 110 °C (ferrocene/ferrocenium was used as internal standard and set at +0.6 V); <sup>c)</sup>By DPV in *o*-C<sub>6</sub>H<sub>4</sub>Cl<sub>2</sub> at 25 °C; <sup>d)</sup>From ref. [14a].

calculated from the onset of the optical absorption (2.5–3.1 eV) increase in the order: DFPT-TTA < DFPT-DTT < DFPT-TT < DFP-TTA < DFP-DTT, as shown in Table 1. This result indicates that electrons are more delocalized as the size of the thiophene core increases (DFP-DTT → DFP-TTA, DFPT-TT → DFPT-DTT → DFPT-TTA) and as additional thienyl units are added to the fused molecular core in the DFP series versus the DFPT series. In view of the larger bandgaps and lower HOMO energies ( $E_{HOMO}$ , vide infra), the end-capped DFPT compounds are projected to have greater ambient oxidative stability than pentacene.<sup>[19]</sup> Thus, the photooxidative stability of the three fused thiophene derivatives was investigated by monitoring the optical absorbance decay at  $\lambda_{max}$  in aerated C<sub>6</sub>H<sub>5</sub>Cl solutions, exposed to white light (a fluorescent lamp) at room temperature. No decomposition was observed for these compounds over the exposure period of 4 d, demonstrating the favorable ambient stability of these materials.

Due to their pronounced structural rigidity, the end-capped DFPT molecules are likely to exhibit exceptional thermal stability (high melting temperature). Differential scanning calorimetry (DSC) measurements show no obvious thermal transitions below 239 °C, and thermogravimetric analysis evidences only 5% weight loss on heating to 319 °C, as summarized in Table 1. Compared to the DFP-end-capped analogs, all three DFPT-end-capped molecules exhibited higher melting points and higher 5% weight-loss temperatures. As might be expected, the highest molecular weight member of the series, DFPT-TTA, exhibits the highest melting point and 5% weight-loss temperature.

### 2.3. Electrochemical Properties

Differential pulse voltammograms (DPV) of the DFPT-end-capped compounds were recorded in *o*-dichlorobenzene, and the resulting reductive and oxidative potentials are summarized in Table 1.<sup>[29]</sup> The oxidative potentials were collected at 110 °C owing to low solubility of DFPT-TTA. The DPV of DFPT-TTA exhibits an oxidative peak at  $\approx +1.14$  V using ferrocene/ferrocenium as an internal standard (set at +0.6 V), while the oxidation potentials ( $E_{ox}$ ) of DFPT-DTT and DFPT-TT shift to more positive values (DFPT-DTT:  $E_{ox} = +1.22$  V; DFPT-TT:  $E_{ox} = +1.29$  V). Since  $E_{ox}$  values for DFPT-TTA, DFPT-DTT, and DFPT-TT are +1.14, +1.22, and +1.29 V, respectively, the corresponding

$E_{HOMO}$ s are estimated at -5.34, -5.42, and -5.49 eV, respectively, using the relationship,  $E_{HOMO} = -(4.20 + E_{ox})$ . The more highly conjugated DFPT-TTA exhibits a higher HOMO energy than those of DFPT-DTT and DFPT-TT, as shown in Figure 5 (assuming ferrocene/ferrocenium oxidation at 4.8 eV). Overall, the optically/electrochemically derived HOMO–LUMO energy gaps are ranked in the order DFPT-TTA < DFPT-DTT < DFPT-TT < DFP-TTA < DFP-DTT, consistent with the conjugative effects of the aryl substituents. Note that DFPT-TT exhibits higher HOMO values and a lower energy gap than those of DFP-TTA, in line with the optical results (vide supra).

### 2.4. Single Crystal Structure Analysis

Analysis of single crystal molecular packing provides an important foundation for the discussion of molecular ordering in solid films and its influence on electronic structure and charge transport properties. The perfluorinated TTA derivatives DFP-TTA and DFPT-TTA crystallize in the monoclinic space group *P*-2<sub>1</sub>/*c* (Table 2). Similar to other fused thiophenes, the unit cell of DFP-TTA exhibits a commonly observed herringbone packing motif (Figure S1, Supporting Information).<sup>[23,28]</sup> The fluorinated phenyl moiety is slightly twisted with respect to the fused thiophene core, with a dihedral angle of 10.2° (Figure S1B, Supporting Information, Table 3). The interplanar distance between TTA cores is 3.59 Å (Figure S1B, Supporting

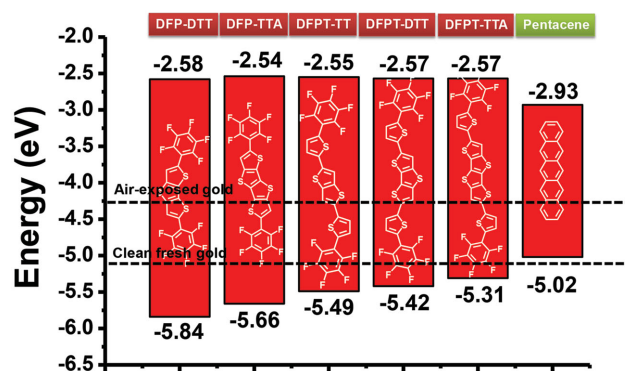


**Figure 5.** Electrochemically derived HOMO and LUMO energy levels of DFPT- and DFP-end-capped organic semiconductors in *o*-C<sub>6</sub>H<sub>4</sub>Cl<sub>2</sub> solution.

**Table 2.** Summary of single crystal cell parameters.

Compound	Crystal system	Space group	<i>a</i> [Å]	<i>b</i> [Å]	<i>c</i> [Å]	$\alpha$ [°]	$\beta$ [°]	$\gamma$ [°]
DFP-TTA	Monoclinic	P2 <sub>1</sub> /c	3.93	11.56	20.48	91.01	90.00	90.00
DFP-DTT	Orthorhombic	Pnma	3.88	11.77	37.05	90.00	90.00	90.00
DFPT-TTA	Monoclinic	P2 <sub>1</sub> /c	3.94	11.35	28.50	97.89	90.00	90.00
DFPT-DTT	Triclinic	P1	6.10	12.60	16.39	101.62	92.73	92.44
DFPT-TT	Triclinic	P1	4.78	6.38	18.33	97.39	91.81	99.47

Information), and the shortest intermolecular sulfur-sulfur distance is 3.58 Å (Figure S1C, Supporting Information). DFPT-TTA exhibits a very similar herringbone packing motif (Figure 6, Table 3, and Table S1, Supporting Information) with a dihedral angle of  $\approx 12^\circ$  (Figure 6B). The shortest interplanar distance between TTA cores is 3.57 Å (Figure 6C) and the shortest sulfur-sulfur distance is 3.50 Å (Figure 6D). Note that the capped phenyl–thiophenyl groups in all three DFPTs are joined in opposite directions with 0–2° dihedral angles to the center fused thiophene cores, affording a nearly coplanar structures. The planar molecular structures and short packing distances of both DFP-TTA and DFPT-TTA suggest favorable conditions to achieve very good charge transport in solid films ( $\mu = 0.30 \text{ cm}^2 \text{ V}^{-1} \text{ s}^{-1}$  for DFP-TTA<sup>[28]</sup> and  $\mu = 0.43 \text{ cm}^2 \text{ V}^{-1} \text{ s}^{-1}$  for DFPT-TTA in thin film transistor measurements, as shown in Table 3).

In general, DFP-DTT exhibits a very similar crystal structure to DFP-TTA and DFPT-TTA.<sup>[25]</sup> DFP-DTT also possesses a typical herringbone packing structure (Tables 2 and 3, Figure S2, Supporting Information).<sup>[25]</sup> The perfluorophenyl groups are only slightly rotated at angles of 11.1° with respect to the DTT core (Figure S2B, Supporting Information). The interplanar distance between the planar DTT cores is 3.60 Å (Figure S2B, Supporting Information) with the shortest sulfur-sulfur distance being 3.48 Å (Figure S2C, Supporting Information). Charge transport in herringbone packing structures is not limited to parallel molecules, but can also occur between diagonally aligned adjacent molecules.<sup>[30–33]</sup> Regardless, the large herringbone angles of DFP-TTA (131.8°), DFP-DTT (136.3°), and DFPT-TTA (129.3°) crystals provide little prospect for charge transport in this alternative pathway. Therefore,  $\pi$ -orbital interactions between parallel/cofacial adjacent molecules are considered to be the major source of charge transport in these crystals, and their packing motifs suggest favorable conditions for  $\pi$ - $\pi$  interaction. For example, the pitch angles of DFP-TTA,

DFP-DTT, and DFPT-TTA are all 0°, which means that the adjacent molecules in these packing motifs are not displaced along the direction of the long molecular axes.<sup>[34]</sup> The roll angles of DFP-TTA, DFP-DTT, and DFPT-TTA are 25°, 22°, and 28°, respectively, implying relatively small displacements along the short molecular axes.<sup>[34]</sup> Thus, this packing configuration provides significant degrees of spatial overlap between adjacent molecular planes.

DFPT-DTT and DFPT-TT have packing structures distinct from typical herringbone packing motifs.<sup>[35]</sup> Both exhibit cofacial nearest-neighbor packing with cell parameters  $a = 6.0988 \text{ Å}$ ,  $b = 12.5964 \text{ Å}$ ,  $c = 16.3881 \text{ Å}$ ,  $\alpha = 101.617^\circ$ ,  $\beta = 92.732^\circ$ ,  $\gamma = 92.446^\circ$ , and  $Z = 2$  for DFPT-DTT (Figure 7, Table 2, and Table S2, Supporting Information) and  $a = 4.7772 \text{ Å}$ ,  $b = 6.3940 \text{ Å}$ ,  $c = 18.3339 \text{ Å}$ ,  $\alpha = 97.385^\circ$ ,  $\beta = 91.813^\circ$ ,  $\gamma = 99.474^\circ$ , and  $Z = 1$  for DFPT-TT (Figure 8, Table 2, and Table S3, Supporting Information). The increased degree of  $\pi$ - $\pi$  overlap in cofacial packing structures is thought to promote more efficient charge transport versus herringbone packing structures.<sup>[17,36,37]</sup> However, the large pitch angles of DFPT-DTT and DFPT-TT indicate that their cofacial structures have a largely head-to-tail arrangement rather than an ideal parallel alignment.

## 2.5. Semiconductor Thin Film Growth

The TFT properties of the new organic semiconductors were investigated on bare doped Si/SiO<sub>2</sub> (gate/insulator) substrates as well as after two different gate dielectric surface treatments. Hexamethyldisilazane (HMDS)-modified substrates were prepared by exposing the Si/SiO<sub>2</sub> substrates to HMDS vapor for 7 d in an N<sub>2</sub> atmosphere, to yield a trimethylsilyl-coated surface. Octadecyltrichlorosilane (OTS)-modified substrates were fabricated by immersion of the Si/SiO<sub>2</sub> substrates in  $3.0 \times 10^{-3} \text{ M}$  hexane solutions of the silane reagent in air after

**Table 3.** Summary of single crystal parameters and thin film transistor electron mobilities.

Compound	Mobility [cm <sup>2</sup> V <sup>-1</sup> s <sup>-1</sup> ]	Nearest-neighbor packing type	Herringbone angle [°]	Intraplanar angle [°]	Roll angle <sup>a)</sup> [°]	Pitch angle <sup>a)</sup> [°]	$\pi$ - $\pi$ distance [Å]	S-S distance [Å]	Density [g cm <sup>-3</sup> ]
DFP-TTA	0.30	Herringbone	131.8	10	25	0	3.59	3.58	2.086
DFP-DTT	0.07	Herringbone	136.3	11	22	0	3.60	3.48	2.073
DFPT-TTA	0.43	Herringbone	129.3	12	28	0	3.57	3.50	1.968
DFPT-DTT	0.09	Cofacial	0	6.5	22	54	3.55	3.45	1.870
DFPT-TT	0.33	Cofacial	0	12	18	44	3.57	3.53	1.935

<sup>a)</sup>Ref. [23].

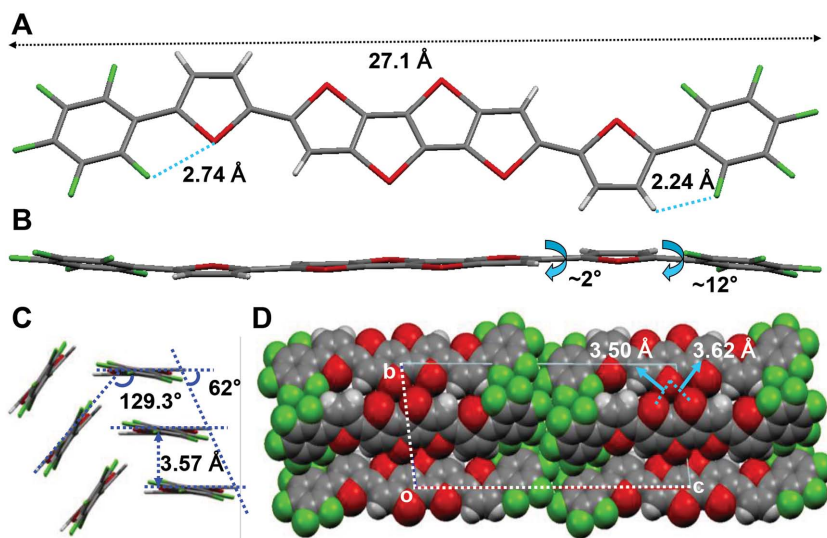


**Figure 6.** The single crystal structure of DFPT-TTA. A) The molecular length of DFPT-TTA is 27.1 Å. B) Side view of DFPT-TTA molecule, with tilting angle between TTA cores and perfluorophenyl group of  $\approx 12^\circ$ . C) Unit cell packing viewed along a  $\pi$ -plane dissection, with herringbone angle of  $129.3^\circ$  between TTA cores, 3.57 Å of layer distance between TTA cores, tilting angle between slipping angle between adjacent molecules in the direction of the short molecular axis is  $62^\circ$ , and thus the roll angle is  $90^\circ - 62^\circ = 28^\circ$ . D) Space filling model of stacking DFPT-TTA molecules. The shortest sulfur-sulfur distance is 3.50 Å; unit cell packing viewed along the  $a$ -axis exhibits no shift between adjacent molecules in the direction of the long molecular axis. The red, dark gray, green, and gray colored bars indicate sulfur, carbon, fluorine, and hydrogen atoms, respectively.

10 h of solution aging under 55–60% of relative humidity. All substrates were characterized by advancing aqueous contact angle measurements, which indicate increasing hydrophobicity in the order: Si/SiO<sub>2</sub> ( $<20^\circ$ ), HMDS-treated Si/SiO<sub>2</sub> ( $95^\circ$ ), OTS-treated Si/SiO<sub>2</sub> ( $104^\circ$ ). The surface roughness was

assayed by tapping mode AFM, revealing a root-mean-square (RMS) roughness of 0.15 nm for SiO<sub>2</sub>, 0.20 nm for HMDS-treated Si/SiO<sub>2</sub>, and 0.35 nm for OTS-treated Si/SiO<sub>2</sub>. All semiconductor films ( $\approx 50$  nm thick) were vapor-deposited at a deposition flux rate of  $0.1 \text{ \AA s}^{-1}$  while maintaining the substrates at temperatures ( $T_d$ ) of 25, 80, or  $110^\circ\text{C}$ . All films were characterized by grazing incidence wide-angle X-ray scattering (GIWAXS) and by tapping mode AFM.

## 2.6. GIWAXS Analysis of Semiconductor Thin Films

GIWAXS data for each semiconducting molecular thin film are shown in Figure 9. The samples investigated by GIWAXS were those that exhibited the best TFT performance (vide infra), which were those with the semiconductor deposited on OTS-functionalized substrates and at an optimal deposition temperature of 25 or  $110^\circ\text{C}$ . Our previous report<sup>[23]</sup> established that thin film organic semiconductors of this general type crystallize with lattice parameters that are similar to, but not identical to, the lattice parameters of the corresponding bulk single crystals. This observation is again made here. For DFP-TTA and DFP-DTT, GIWAXS patterns for nominally 50 nm thick films on OTS/SiO<sub>2</sub>/Si at  $25^\circ\text{C}$  (Figure 9A,B), show a series of discrete diffraction spots at different  $q_z$  values for specific  $q_{xy}$ . The diffraction spots can be indexed according to the corresponding bulk single crystal structure forms. Such indexing reveals that the crystallites are oriented with the (0 0 1) axis parallel to the surface normal. However, for both DFP-TTA and DFP-DTT, the in-plane lattice parameters of the thin film unit cells are contracted by  $\approx 7\%$ – $9\%$  along both the  $a$ - and  $b$ -axes versus their bulk single crystal forms. Giri et al. showed this type of lattice strain can greatly affect carrier mobility in TIPS-pentacene films.<sup>[38]</sup> Furthermore, note that these diffraction patterns are independent of the sample azimuthal orientation. This observation indicates that these films are 2D powders, that is, the film consists of crystallites oriented with the long molecular axes parallel to the surface normal, but with no preferred in-plane orientation.

As the long axis lengths of the present semiconducting molecules increase, the thin film morphologies transition from crystalline 2D powders to preferentially oriented 3D crystallites. This is particularly evident for DFPT-DTT and DFPT-TTA (Figure 9D,E), which are the two longest molecules in the current study. Specifically, for thin films of these

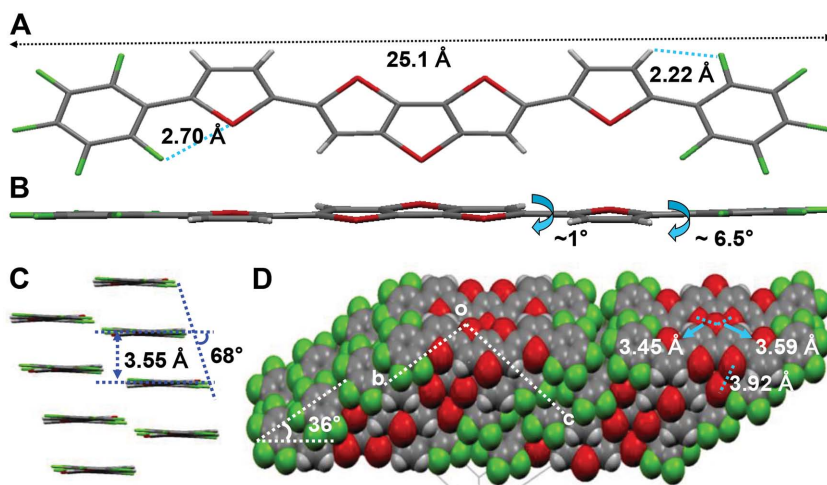


**Figure 7.** Single crystal structure of DFPT-DTT. A) The molecular length of DFPT-DTT is 25.1 Å. B) Side view of DFPT-DTT molecule, with tilting angle between TTA cores and perfluorophenyl group of  $\approx 6.5^\circ$ . C) Unit cell packing viewed along a  $\pi$ -plane dissection, with cofacial packing, with herringbone angle between DTT cores equal to  $0^\circ$ , layer distance between DTT cores is 3.55 Å, slipping angle in the direction of the short molecular axis is  $68^\circ$ , and thus the roll angle is  $90^\circ - 68^\circ = 22^\circ$ . D) Space filling model of stacking DFPT-DTT molecules. The slipping angle in the direction of the long molecular axis is  $36^\circ$ , and thus the pitch angle is  $90^\circ - 36^\circ = 54^\circ$ . The shortest sulfur-sulfur distance is 3.45 Å. The red, dark gray, green, and gray colored bars indicate sulfur, carbon, fluorine, and hydrogen atoms, respectively.

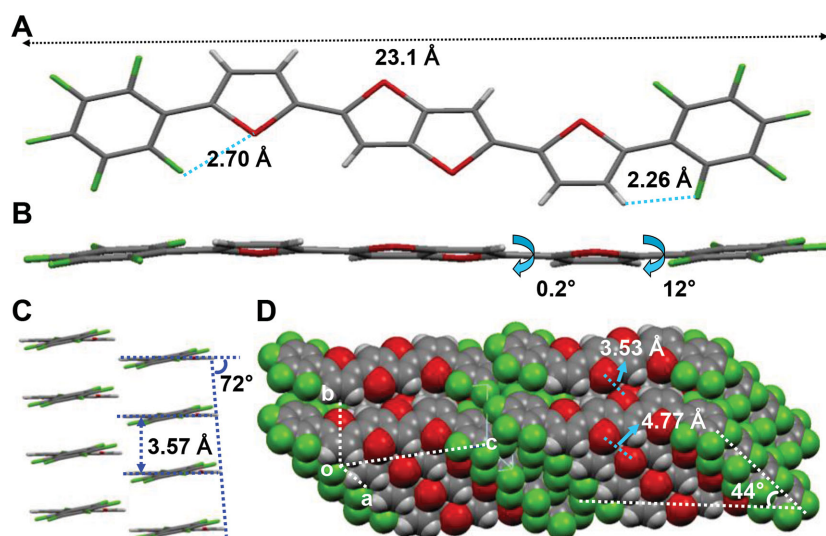


**Figure 8.** Single crystal structure of DFPT-TT. A) The molecular length of DFPT-TT is 23.1 Å. B) Side view of DFPT-TT molecule, with tilting angle between TTA cores and perfluorophenyl group of 12°. C) Unit cell packing viewed along a  $\pi$ -plane dissection cofacial packing, with herringbone angle between TT cores equal to 0°, layer distance between TT cores is 3.57 Å, slipping angle in the direction of the short molecular axis is 72°, and thus, the roll angle is  $90^\circ - 72^\circ = 18^\circ$ . D) Space filling model of stacking DFPT-TT molecules. The slipping angle in the direction of the long molecular axis is 46°, and thus the pitch is  $90^\circ - 46^\circ = 44^\circ$ . The shortest sulfur-sulfur distance is 3.53 Å. The red, dark gray, green, and gray colored bars indicate sulfur, carbon, fluorine, and hydrogen atoms, respectively.

molecules, the scattered intensity is distributed along Debye–Scherrer rings. The sharp diffraction spots present on Debye–Scherrer rings indicate that the crystallites are, on average, not randomly oriented, but have a crystallographic axis preferentially aligned along the substrate normal. However, for these molecules, the  $q$ -positions of the Debye–Scherrer rings could not be indexed using the bulk single crystal lattice parameters.

The case of the third longest molecule DFPT-TT is intermediate between DFP-TTA and DFPT-TTA. Specifically, for this molecule, 2D and 3D powders coexist, as evidenced by the presence of series of discrete diffraction spots at different

$q_z$  values for specific  $q_{xy}$  and Debye–Scherrer rings within the same GIWAXS pattern (Figure 9C). However, note that all of the discrete diffraction spots do not lie on the same Debye–Scherrer ring, indicating that the 2D and the preferentially oriented 3D powder patterns correspond to distinct crystallographic forms. In general, the GIWAXS pattern for DFPT-TT is dense with diffraction spots and rings, which for the time being has made accurate indexing of the pattern unfeasible. To summarize, the key qualitative finding of the present GIWAXS measurements is that shorter molecules form crystallites that have one crystallographic axis perfectly oriented with respect to the substrate normal. Moreover, this preferred orientation diminishes with molecular length.

## 2.7. Optical Absorption Spectra of Organic Semiconductor Thin Films

The optical absorption maximum of a molecular solid can be displaced to either a shorter or longer wavelength versus the corresponding absorption spectrum in solution.

Materials exhibiting blue-shifted maxima (hypsochromic shift) are defined as having an H-aggregate microstructure,<sup>[7,39–41]</sup> while those exhibiting a red-shift (bathochromic shift) absorption have a J-aggregate microstructure.<sup>[42–45]</sup> The origin of the H- or J-type spectral shift can be understood as follows:<sup>[46]</sup> each molecule can be approximated as a point dipole (with dipole moments  $\mu_1$  and  $\mu_2$ ), and the potential energy ( $V$ ) of interaction between two molecules is a function of their relative dipole slip angle ( $\theta$ ), where a head-to-tail alignment is defined as  $\theta = 0^\circ$  and a parallel alignment, head-to-head, is defined as  $\theta = 90^\circ$ . According to the relationship<sup>[46]</sup>  $V = \frac{\mu_1 \mu_2}{4\pi\epsilon_0 r^3} (1 - 3\cos^2(\theta))$ , where  $\epsilon_0$  is the permittivity of

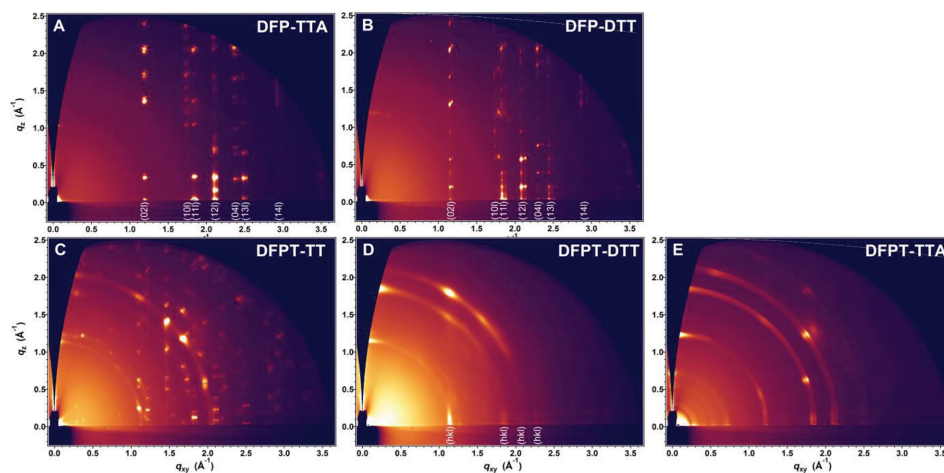


**Figure 9.** Comparison of GIWAXS data for DFPT and DFP thin films grown at the indicated temperatures: A) DFP-TTA 25 °C, B) DFP-DTT at 25 °C, C) DFPT-DTT at 25 °C, D) DFPT-TT at 25 °C, and E) DFPT-TTA at 110 °C.

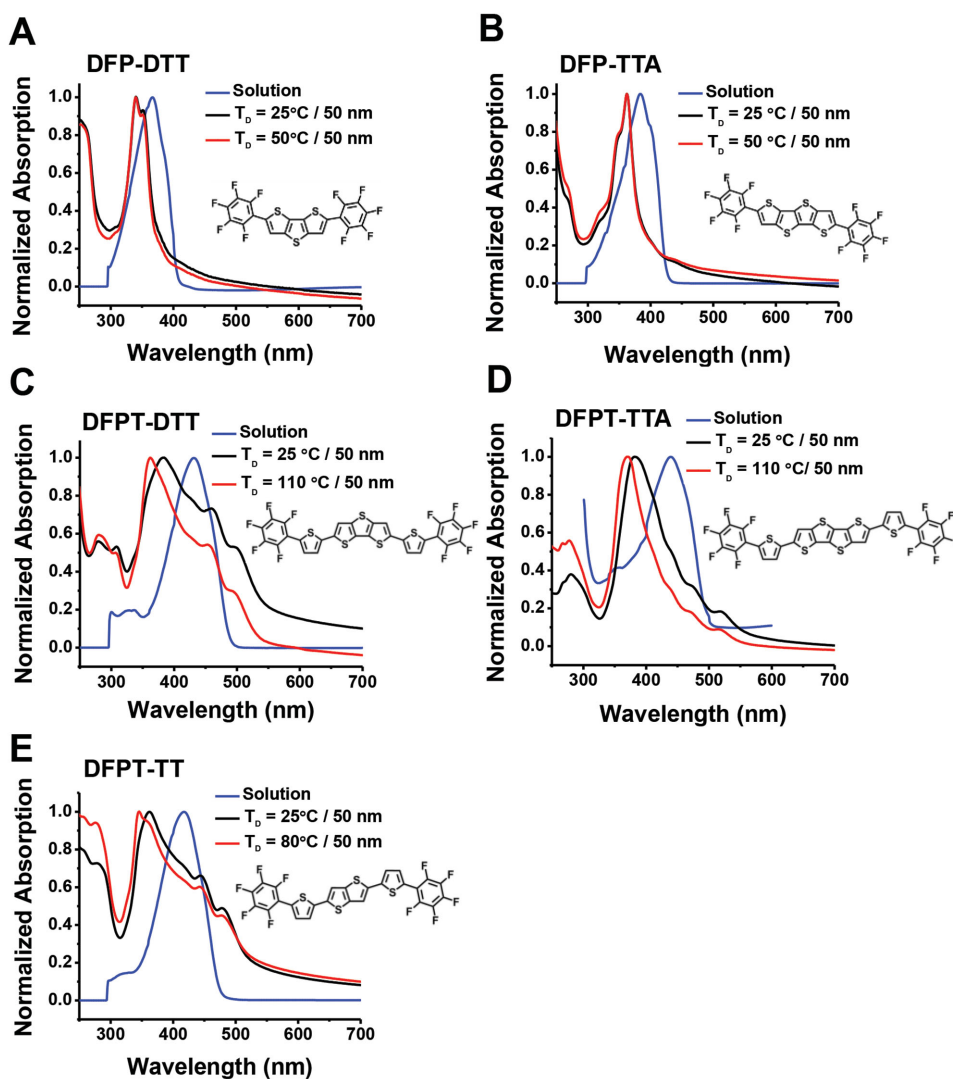


**Figure 10.** Comparison of the optical absorption spectra in solution and thin films: A) DFP-DTT, B) DFP-TTA, C) DFPT-DTT, D) DFPT-TTA, and E) DFPT-TT.

free space and  $r$  is the distance between the molecules, if the two dipoles are aligned with  $\theta < 54.74^\circ$  and  $V < 0$ , then the optical absorption spectrum exhibits a hypsochromic shift, and if the two dipoles are aligned with  $\theta > 54.74^\circ$  and  $V > 0$ , then the spectrum exhibits a bathochromic shift. Structurally, the area of  $\pi$ -overlap between adjacent molecules is greater in H-aggregates than in J-aggregates if the molecular structure is similar in both the molecular solids. In the present study, we find that the UV-vis absorption maxima are blue-shifted in each case with respect to DFP-TTA, DFP-DTT, and DFPT-TTA, and exhibit an H-type packing structures, whereas DFPT-DTT and DFPT-TT exhibit J-type packing (Figure 10 and Table 4).

Onset wavelengths determined by the intersection of two tangents on the absorption edges of thin film of optical spectra provide clear metrics for discussing bandgap energy trends, because the molecular electron excitation occurs at the energy corresponding to the onset wavelength. Although the absorption maxima of DFP-DTT, DFP-TTA, DFPT-TTA, DFPT-DTT, and DFPT-TT films are all displaced to shorter wavelength

**Table 4.** Summary of UV-vis absorption spectra in solution and in thin film.

Compound	Sample <sup>a)</sup>	$\lambda_{\text{on-set}}$ [nm]	$\lambda_{\text{max}}$ [nm]	$E_g^{\text{opt b)}$ [eV]
DFP-DTT	Solution	405	367	3.06
	Film	372	340	3.33
DFP-TTA	Solution	423	384	2.93
	Film	380	362	3.26
DFPT-TTA	Solution	495	439	2.51
	Film	461	381	2.69
DFPT-DTT	Solution	487	432	2.55
	Film	538	383	2.30
DFPT-TT	Solution	477	418	2.60
	Film	512	362	2.42

<sup>a)</sup>Thin films deposited at both 25 and 50 °C exhibit identical optical absorption;

<sup>b)</sup>Optical bandgap,  $E_g^{\text{opt}}$ , calculated from  $\lambda_{\text{on-set}}$ .

versus their absorption maxima in solution (Figure 10), the direction of the onset wavelength shift divides the present semiconductors into two groups: the onset wavelengths of DFP-DTT, DFP-TTA, and DFPT-TTA decrease from 405, 423, and 495 nm (solution) to 372, 380, and 460 nm (thin film), respectively (Figure 10, Table 3). In contrast, the onset wavelengths of DFPT-DTT and DFPT-TT increase from 487 and 476 nm (solution) to 538 and 512 nm (thin film), respectively (Figure 10, Table 3). Therefore, the bandgaps of the first group of semiconductor molecules increases from 3.06, 2.93, and 2.51 eV (solution) to 3.33, 3.26, and 2.69 eV (thin film) while the bandgaps of the second semiconductor group decrease from 2.55 and 2.60 eV (solution) to 2.30 and 2.42 eV (thin film). Interestingly, the absorption maxima of DFPT-TTA, DFPT-DTT, and DFPT-TT films are all displaced to shorter wavelength at higher deposition temperatures, which might indicate temperature-dependent film texturing (vide infra).

The above results strongly suggest that DFP-DTT, DFP-TTA, and DFPT-TTA form optical H-aggregates in thin films while DFPT-DTT and DFPT-TT form optical J-aggregates, and that these differences arise from the differences in molecular packing motifs. Assuming the molecules arrange in thin films with the same (or very similar) packing motifs as those in the corresponding bulk crystals, then the analysis of bulk crystal structures should provide the structural origin of these optical effects. Thus, from the single crystal structural data, DFP-DTT, DFP-TTA, and DFPT-TTA thin films should exhibit negligible optical shifts between adjacent molecules in the molecular long axis direction, and exhibit relatively small shifts in the short molecular axis direction based on the 0° pitch angles and small roll angles. This parallel arrangement of closely packed neighboring molecules significantly increases the transition dipole coupling, inducing a transition to a higher excitonic energy state than for the isolated molecules, reasonably approximated by the transition energy in solution. In the same vein, the thin films of DFPT-DTT and DFPT-TT will have relatively large shifts between adjacent molecules in the molecular long axis direction, consistent with the large pitch angles. This head-to-tail arrangement of molecular packing reduces the transition dipole coupling between molecules, and decreases the excitonic state energy. Therefore, the pitch angles from the previous bulk crystal structural analysis are key parameters for determining whether the molecular aggregation consists of H-aggregates or J-aggregates, assuming that the thin film packing motifs are similar to those in the bulk crystals.

## 2.8. OTFT Fabrication and Characterization

Thin film transistors were fabricated in a bottom gate-top contact configuration. Highly doped p-type (100) silicon wafers were used as gate electrodes as well as substrates, and thermally grown 300 nm thick SiO<sub>2</sub> on the Si was used as the gate insulator. Organic semiconductor thin films (50 nm) were vapor-deposited onto Si/SiO<sub>2</sub>, HMDS-treated Si/SiO<sub>2</sub>, and OTS-treated Si/SiO<sub>2</sub> substrates maintained at specific deposition temperatures (*T<sub>D</sub>*). Next, 50 nm thick gold source and drain electrodes were vapor-deposited at 2 × 10<sup>-6</sup> Torr through a shadow mask in a high vacuum deposition chamber. Devices were fabricated with a channel length of 100 μm and a channel

width of 5000 μm. Current-voltage (*I*-*V*) transfer and output plots were measured for each device under vacuum and in air. Key device performance parameters, such as field-effect mobility ( $\mu$ ), threshold voltage (*V<sub>T</sub>*), and current on-to-off ratio (*I<sub>on</sub>*/*I<sub>off</sub>*), were extracted using standard procedures.<sup>[47]</sup> The results are summarized in Table 5. Output and transfer plots are shown in Figure 11.

OTFTs fabricated with DFPT-TTA and DFPT-TT exhibit good n-type charge transport properties in vacuum.<sup>[48]</sup> DFPT-TTA devices grown on OTS-treated substrates at 110 °C exhibit the best device performance with  $\mu = 0.43 \text{ cm}^2 \text{ V}^{-1} \text{ s}^{-1}$  and *I<sub>on</sub>*/*I<sub>off</sub>* = 3.7 × 10<sup>8</sup>. DFPT-TT devices on OTS-treated substrates grown at 25 °C exhibit comparable performance,  $\mu = 0.33 \text{ cm}^2 \text{ V}^{-1} \text{ s}^{-1}$  and *I<sub>on</sub>*/*I<sub>off</sub>* = 1.8 × 10<sup>8</sup> (Table 5). In contrast, relatively poor device performance is observed for films of DFPT-DTT with  $\mu = 0.086 \text{ cm}^2 \text{ V}^{-1} \text{ s}^{-1}$ , *I<sub>on</sub>*/*I<sub>off</sub>* = 3.3 × 10<sup>7</sup> grown on OTS-treated substrates at 25 °C. The effect of the substrate temperature during semiconductor growth on the TFT performance in vacuum depends on the type of semiconductor. As the growth temperature is increased, the electron mobility of the DFPT-TTA devices increase from  $\mu = 4.3 \times 10^{-5} \text{ cm}^2 \text{ V}^{-1} \text{ s}^{-1}$  at 25 °C to 0.43 cm<sup>2</sup> V<sup>-1</sup> s<sup>-1</sup> at 110 °C on OTS-treated substrates. In contrast, the mobilities of the DFPT-DTT and DFPT-TT TFTs decrease as the growth temperature is increased from  $\mu = 0.086 \text{ cm}^2 \text{ V}^{-1} \text{ s}^{-1}$  at 25 °C to  $\mu = 0.056 \text{ cm}^2 \text{ V}^{-1} \text{ s}^{-1}$  at 110 °C for DFPT-DTT and  $\mu = 0.33 \text{ cm}^2 \text{ V}^{-1} \text{ s}^{-1}$  at 25 °C to  $\mu = 0.12 \text{ cm}^2 \text{ V}^{-1} \text{ s}^{-1}$  at 80 °C for DFPT-TT, respectively.

Since the out-of-plane X-ray diffraction data show that film crystallinity increases with increasing substrate temperature during film growth (Figures S3, S5, and S7, Supporting Information), a possible origin of this mobility degradation may be decreased film grain interconnectivity (vide infra). Polycrystalline films are composed of crystalline domains, amorphous boundary regions, and grain boundaries. These boundary regions are known to disrupt charge flow as a result of structural discontinuities and charge traps residing in these sites.<sup>[49-51]</sup> As the crystallite grain size of the semiconductor film increases with the substrate temperature, the size of the grain boundaries also grows proportionally to the grain sizes. AFM images indicate that DFPT-TTA films are composed of thin, wire-like grains (Figure S9, Supporting Information), while DFPT-DTT and DFPT-TT films exhibit large plate-like grains (Figures S10 and S11, Supporting Information) when grown at high substrate temperatures. Therefore, growing grain boundaries and the resulting degradation of film interconnectivity is more severe in DFPT-DTT and DFPT-TT films than in DFPT-TTA films. This point is discussed in more detail below.

The effect of SiO<sub>2</sub> gate dielectric SAM (self-assembled monolayers) coating is consistent within the present semiconductor series. Among the three substrate types, OTS-treated substrates consistently afford the best device performance, followed by HMDS, and then untreated SiO<sub>2</sub>. For DFPT-TTA, the mobility is 0.055 cm<sup>2</sup> V<sup>-1</sup> s<sup>-1</sup> on bare SiO<sub>2</sub>, 0.11 cm<sup>2</sup> V<sup>-1</sup> s<sup>-1</sup> on HMDS-treated Si/SiO<sub>2</sub>, and 0.43 cm<sup>2</sup> V<sup>-1</sup> s<sup>-1</sup> on OTS-treated Si/SiO<sub>2</sub> for 110 °C growth. DFPT-DTT devices exhibit  $\mu = 0.0054 \text{ cm}^2 \text{ V}^{-1} \text{ s}^{-1}$  on bare SiO<sub>2</sub>, 0.03 cm<sup>2</sup> V<sup>-1</sup> s<sup>-1</sup> on HMDS-treated Si/SiO<sub>2</sub>, and 0.086 cm<sup>2</sup> V<sup>-1</sup> s<sup>-1</sup> on OTS-treated Si/SiO<sub>2</sub> for 25 °C growth. DFPT-TT devices exhibit  $\mu = 0.095 \text{ cm}^2 \text{ V}^{-1} \text{ s}^{-1}$  on bare SiO<sub>2</sub>, 0.16 cm<sup>2</sup> V<sup>-1</sup> s<sup>-1</sup> on HMDS-treated Si/SiO<sub>2</sub>, and

**Table 5.** TFT device performance parameters of DFPT-end-capped compounds employed in this study ( $T_D$ : substrate temperature,  $\mu$ : carrier mobility,  $V_T$ : threshold voltage,  $I_{on}/I_{off}$ : current on/off ratio).

Compound	$T_D^{a)}$ [°C]	Surface treatment	Vacuum				Air			
			Carrier sign	$\mu^{b)}$ [cm <sup>2</sup> V <sup>-1</sup> s <sup>-1</sup> ]	$V_T$ [V]	$I_{on}/I_{off}$	Carrier sign	$\mu^{b)}$ [cm <sup>2</sup> V <sup>-1</sup> s <sup>-1</sup> ]	$V_T$ [V]	$I_{on}/I_{off}$
DFPT-TTA	25	Bare	N	$(9.9 \pm 1.1) \times 10^{-4}$ Max = 0.0011	$73 \pm 1$	$(8.6 \pm 3.1) \times 10^4$		NA <sup>c)</sup>		
		HMDS	N	$(8.3 \pm 0.4) \times 10^{-3}$ Max = 0.0087	$61 \pm 2$	$(3.7 \pm 1.9) \times 10^6$		NA		
		OTS	N	$(6.4 \pm 1.8) \times 10^{-2}$ Max = 0.082	$45 \pm 10$	$(2.0 \pm 0.0) \times 10^7$		NA		
	80	Bare	N	$(2.3 \pm 0.4) \times 10^{-4}$ Max = 0.00027	$66 \pm 7$	$(6.9 \pm 3.1) \times 10^6$		NA		
		HMDS	N	$(3.6 \pm 0.6) \times 10^{-4}$ Max = 0.00042	$57 \pm 3$	$(2.6 \pm 0.7) \times 10^7$		NA		
		OTS	N	$(5.8 \pm 0.9) \times 10^{-4}$ Max = 0.00067	$41 \pm 2$	$(6.0 \pm 2.8) \times 10^7$		NA		
	110	Bare	N	$0.052 \pm 0.003$ Max = 0.055	$67 \pm 6$	$(3.0 \pm 1.1) \times 10^7$		NA		
		HMDS	N	$0.093 \pm 0.016$ Max = 0.11	$58 \pm 5$	$(2.3 \pm 1.6) \times 10^6$		NA		
		OTS	N	$0.40 \pm 0.03$ Max = 0.43	$54 \pm 7$	$(2.6 \pm 1.3) \times 10^8$		NA		
DFPT-DTT									NA	
DFPT-DTT	25	Bare	N	$(4.6 \pm 0.8) \times 10^{-3}$ Max = 0.0054	$85 \pm 10$	$(3.4 \pm 2.3) \times 10^5$		NA		
		HMDS	N	$0.027 \pm 0.003$ Max = 0.030	$67 \pm 4$	$(2.1 \pm 1.1) \times 10^6$	P	$(4.0 \pm 0.8) \times 10^{-5}$ Max = $4.8 \times 10^{-5}$	$-(78 \pm 3)$	$(3.6 \pm 1.1) \times 10^3$
		OTS	N	$0.076 \pm 0.012$ Max = 0.086	$32 \pm 0$	$(2.9 \pm 0.0) \times 10^5$	P	$(3.5 \pm 1.3) \times 10^{-4}$ Max = $4.8 \times 10^{-4}$	$-(48 \pm 11)$	$(2.6 \pm 0.8) \times 10^4$
	80	Bare	N	$(1.7 \pm 0.2) \times 10^{-6}$ Max = $1.9 \times 10^{-6}$	$77 \pm 2$	$(3.6 \pm 0.5) \times 10^3$		NA		
		HMDS	N	$0.031 \pm 0.013$ Max = 0.044	$63 \pm 6$	$(1.1 \pm 0.4) \times 10^4$	P	$(1.0 \pm 0.7) \times 10^{-5}$ Max = $1.7 \times 10^{-5}$	$-(63 \pm 6)$	$16 \pm 2$
		OTS	N	$0.010 \pm 0.000$ Max = 0.010	$40 \pm 7$	$(3.2 \pm 0.3) \times 10^6$	P	$(1.3 \pm 0.0) \times 10^{-5}$ Max = $1.3 \times 10^{-5}$	$-(21 \pm 0)$	$12 \pm 0$
	110	Bare	N	$(1.5 \pm 0.0) \times 10^{-5}$ Max = $1.5 \times 10^{-5}$	$93 \pm 0$	$(9.5 \pm 0.0) \times 10^3$		NA		
		HMDS	N	$0.015 \pm 0.000$ Max = 0.015	$55 \pm 1$	$(3.2 \pm 3.0) \times 10^6$	P	$(9.1 \pm 1.8) \times 10^{-6}$ Max = $1.1 \times 10^{-5}$	$-(26 \pm 4)$	$(1.7 \pm 0.2) \times 10^3$
		OTS	N	$0.055 \pm 0.001$ Max = 0.056	$42 \pm 3$	$(4.9 \pm 2.9) \times 10^7$	P	$(6.1 \pm 0.9) \times 10^{-4}$ Max = $7.0 \times 10^{-4}$	$-(29 \pm 7)$	$(3.1 \pm 2.5) \times 10^4$

continued

**Table 5.** Continued

Compound	$T_D^{a)}$ [°C]	Surface treatment	Vacuum				Air			
			Carrier sign	$\mu^b)$ [cm <sup>2</sup> V <sup>-1</sup> s <sup>-1</sup> ]	$V_T$ [V]	$I_{on}/I_{off}$	Carrier sign	$\mu^b)$ [cm <sup>2</sup> V <sup>-1</sup> s <sup>-1</sup> ]	$V_T$ [V]	$I_{on}/I_{off}$
DFPT-TT							P		-(29 ± 7)	
	25	Bare	N	0.061 ± 0.034 Max = 0.095	50 ± 2	(2.9 ± 1.6) × 10 <sup>8</sup>			NA	
		HMDS	N	0.13 ± 0.03 Max = 0.16	52 ± 8	(6.8 ± 4.0) × 10 <sup>7</sup>			NA	
		OTS	N	0.27 ± 0.06 Max = 0.33	55 ± 6	(2.4 ± 1.7) × 10 <sup>8</sup>			NA	
	80	Bare	N	(1.7 ± 0.9) × 10 <sup>-4</sup> Max = 2.6 × 10 <sup>-4</sup>	79 ± 6	(5.5 ± 2.4) × 10 <sup>3</sup>			NA	
		HMDS	N	0.090 ± 0.007 Max = 0.097	40 ± 1	(3.7 ± 3.6) × 10 <sup>7</sup>			NA	
		OTS	N	0.11 ± 0.01 Max = 0.12	47 ± 7	(8.6 ± 5.0) × 10 <sup>5</sup>			NA	

<sup>a)</sup>Substrate temperature during film growth; <sup>b)</sup>Average values for at least five devices; <sup>c)</sup>Not active.

0.33 cm<sup>2</sup> V<sup>-1</sup> s<sup>-1</sup> on OTS-treated Si/SiO<sub>2</sub> for 25 °C growth. The effect of substrate treatment is well rationalized by the out-of-plane X-ray diffraction data (Figures S4, S6, and S8, Supporting Information). The most intense reflections are observed for the semiconductor films grown on OTS-treated Si/SiO<sub>2</sub> substrates, especially for low temperature growth. Another reason that OTS-treated Si/SiO<sub>2</sub> is particularly effective in achieving superior device performance is explained in terms of semiconductor film morphologies and energetics in the next section (vide infra).

Another noteworthy phenomenon here is that the DFPT-DTT exhibits p-type charge transport in air while exhibiting n-type operation under vacuum (Table 5). The best p-channel mobility in air is  $\approx 7.0 \times 10^{-4}$  cm<sup>2</sup> V<sup>-1</sup> s<sup>-1</sup> for films deposited at 110 °C on OTS-treated substrates. When TFT devices are exposed to ambient atmosphere, charge trap states can be created in electron transporting semiconductors since O<sub>2</sub> and H<sub>2</sub>O are electron acceptors. Furthermore, for materials with low ionization energies, O<sub>2</sub> can also dope the semiconductor or pre-fill hole charge trapping states favoring hole conduction. This hole filling effect of the trap states can lead to high hole field-effect mobilities. For example, Okamoto et al.<sup>[52]</sup> reported for TFT devices fabricated from picene that O<sub>2</sub> exposure can significantly enhance both mobility and on-to-off current ratio. In the present case, the question is whether the mobile hole carriers intrinsically arise from the DFPT-DTT from the field effect, or whether they are induced only upon the presence of H<sub>2</sub>O or O<sub>2</sub>. Relevant to this question we find that the change between p-type and n-type performance differs greatly after storing the DFPT-DTT devices for 70 d in air (Table 6). In the case of n-type operation (measured in vacuum), the mobility is reduced to  $\approx 1/10$ th of the original values. In contrast, the p-type transport is unaffected by air exposure. This observation argues the mobile hole charge carrier states arise from environmental dopants.

## 2.9. Semiconductor Film Morphology, Electronic Structure, and OTFT Performance

While a variety of factors are known to impact TFT performance, semiconductor film morphology induced by a dielectric surface treatment is a key element affecting charge transport. In particular, the morphology of the first few monolayers situated directly above the dielectric is critically important for achieving good device performance since the semiconductor charge transport occurs in this region. It is therefore important to examine the correlation between the microscopic film structure and the macroscopic OTFT performance.

While the evolution of bulk film morphology satisfactorily explains the effects of the substrate temperature on semiconductor film crystallinity (Figures S9–S11, Supporting Information), it does not correlate well with the dielectric surface treatment. For example, the morphologies of 50 nm thick films do not vary greatly between the three different types of substrates. In contrast, AFM images of submonolayer films grown on the different substrates clearly explain the origin of the differences in device performance as a function of dielectric surface treatment (Figures 12–14). The submonolayer semiconductor films on OTS-treated Si/SiO<sub>2</sub> exhibits a higher nucleation density and better surface coverage than the submonolayer films on other substrates for all three compounds. In addition, the grains are more laterally spread rather than vertically aggregated on OTS-treated Si/SiO<sub>2</sub>. Such 2D film growth is beneficial in forming complete charge transport pathways within the first few monolayers of semiconductor films on a TFT dielectric, affording high device performance (vide supra).<sup>[1b]</sup>

In addition to the semiconductor film morphology, the energetics of the semiconductor films were characterized to investigate correlations with device performance. The HOMO

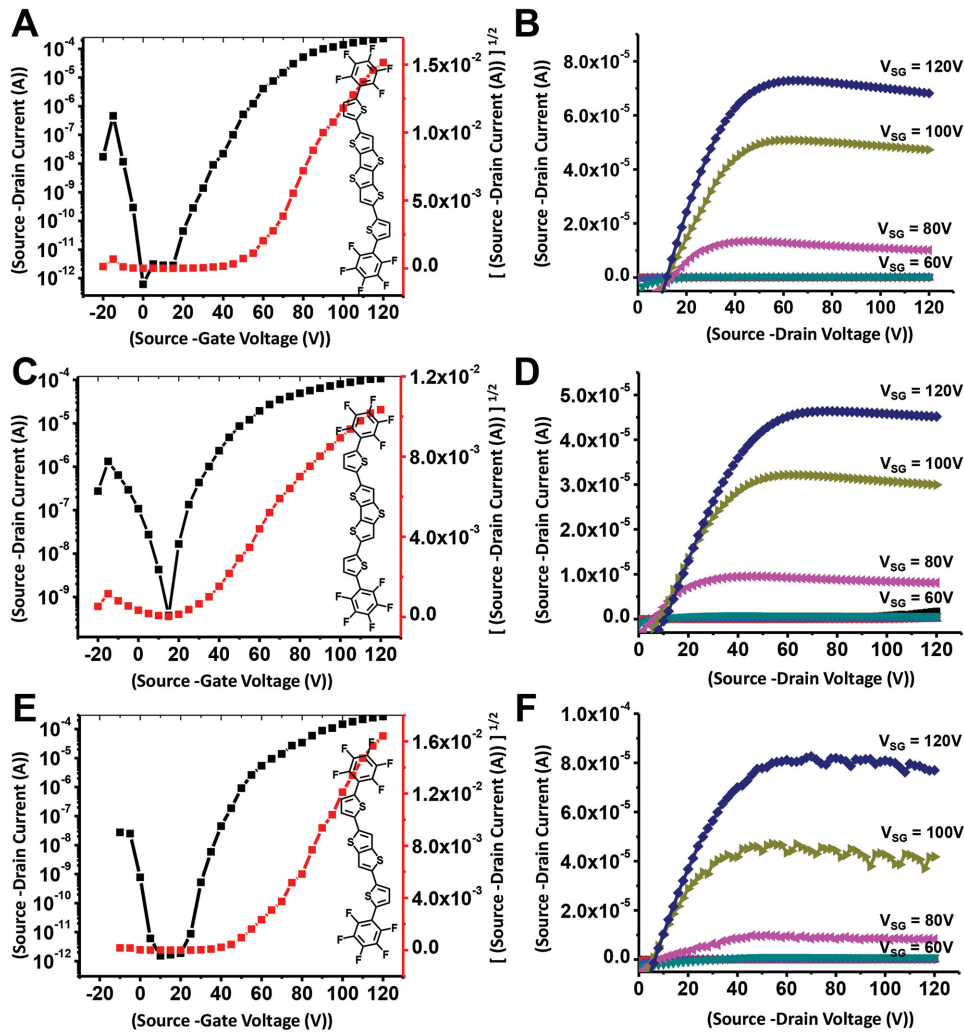


**Figure 11.** Transfer and output plots of OTFT devices fabricated from DFPT-TTA, DFPT-DTT, and DFPT-TT films grown on an OTS-coated substrate: DFPT-TTA ( $T_D = 110\text{ }^\circ\text{C}$ ) A) transfer plot and B) output plot; DFPT-DTT ( $T_D = 25\text{ }^\circ\text{C}$ ) C) transfer plot and D) output plot; DFPT-TT ( $T_D = 25\text{ }^\circ\text{C}$ ) E) transfer plot and F) output plot. The device performances are as follows: DFPT-TTA: n-type,  $\mu = 0.43\text{ cm}^2\text{ V}^{-1}\text{ s}^{-1}$ ,  $V_{th} = 58\text{ V}$ , and  $I_{on}/I_{off} = 3.7 \times 10^5$  under vacuum. DFPT-DTT: n-type,  $\mu = 0.086\text{ cm}^2\text{ V}^{-1}\text{ s}^{-1}$ ,  $V_{th} = 32\text{ V}$ , and  $I_{on}/I_{off} = 2.9 \times 10^5$  under vacuum. DFPT-TT: n-type,  $\mu = 0.33\text{ cm}^2\text{ V}^{-1}\text{ s}^{-1}$ ,  $V_{th} = 60\text{ V}$ , and  $I_{on}/I_{off} = 1.8 \times 10^8$  under vacuum. Deposition flux rate  $0.1\text{ \AA s}^{-1}$ , channel length  $100\text{ }\mu\text{m}$ , and channel width  $5000\text{ }\mu\text{m}$ .

**Table 6.** TFT device performance of DFPT-DTT after 70 d of air exposure ( $T_D$ : substrate temperature,  $\mu$ : carrier mobility,  $V_T$ : threshold voltage,  $I_{on}/I_{off}$ : current on/off ratio).

Compound	$T_D^a$ [ $^\circ\text{C}$ ]	Surface treatment	Vacuum				Air			
			Carrier sign	$\mu^b$ [ $\text{cm}^2\text{ V}^{-1}\text{ s}^{-1}$ ]	$V_T$ [V]	$I_{on}/I_{off}$	Carrier sign	$\mu^a$ [ $\text{cm}^2\text{ V}^{-1}\text{ s}^{-1}$ ]	$V_T$ [V]	$I_{on}/I_{off}$
DFPT-DTT	25	Bare	N	$(3.2 \pm 1.9) \times 10^{-4}$ Max = $5.1 \times 10^{-4}$	$88 \pm 5$	$(3.8 \pm 1.7) \times 10^4$	P	$(4.1 \pm 0.1) \times 10^{-6}$ Max = $4.2 \times 10^{-6}$	$-(12 \pm 0)$	$(8.6 \pm 3.8) \times 10^2$
			N	$(6.0 \pm 1.3) \times 10^{-3}$ Max = $7.3 \times 10^{-3}$	$85 \pm 3$	$(1.6 \pm 0.5) \times 10^5$	P	$(4.4 \pm 2.1) \times 10^{-5}$ Max = $6.5 \times 10^{-5}$	$-(77 \pm 2)$	$(1.0 \pm 0.4) \times 10^4$
			N	$(3.5 \pm 1.5) \times 10^{-3}$ Max = $5.0 \times 10^{-3}$	$60 \pm 8$	$(1.0 \pm 0.4) \times 10^6$	P	$(1.3 \pm 1.2) \times 10^{-4}$ Max = $2.5 \times 10^{-4}$	$-(34 \pm 14)$	$(2.4 \pm 1.7) \times 10^4$

<sup>a)</sup>The average values obtained for at least five devices.

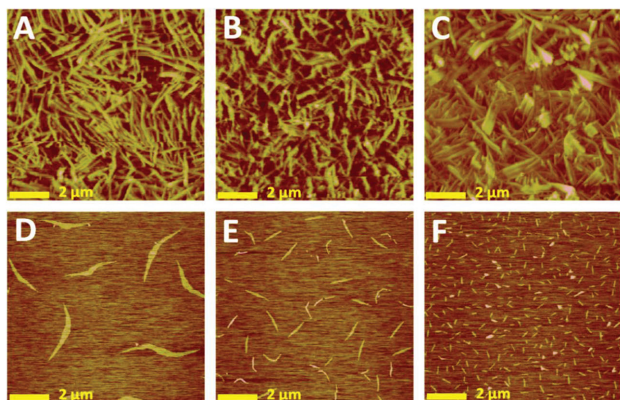


**Figure 12.** Comparison of bulk film and submonolayer film morphology of DFPT-TTA films (AFM images): A) 50 nm, on bare SiO<sub>2</sub>, B) 50 nm, on HMDS-treated Si/SiO<sub>2</sub>, C) 50 nm, on OTS-treated Si/SiO<sub>2</sub>, D) 1.5 nm, on bare SiO<sub>2</sub>, E) 1.5 nm, on HMDS-treated Si/SiO<sub>2</sub>, and F) 1.5 nm, OTS-treated Si/SiO<sub>2</sub>. All films were grown at  $T_D = 110^\circ\text{C}$  ( $10\ \mu\text{m} \times 10\ \mu\text{m}$ ).

and LUMO energies of the semiconductor films were investigated by ultraviolet photoemission spectroscopy (UPS) (Figure 15).<sup>[53–55]</sup> UPS utilizes UV light to excite photoelectrons from shallow valence states, serving as a probe for the valence bands (ionization potential) in solids. Since there was no straightforward method available to us to directly measure the electron affinity, the LUMO energy is estimated here from the HOMO energy and the optical bandgap ( $E_{\text{gap}}$ ) in turn deduced from the optical spectra (Table 4).

It is known that the ionization potential of thin films can be greatly influenced by the underlying semiconductor–dielectric interface.<sup>[56a]</sup> In particular, the surface potential is significantly altered when an organic SAM is introduced on top of the gate dielectric. Here, we focus on the change in the semiconductor film LUMO energy after introducing OTS on the SiO<sub>2</sub> gate dielectric. As shown in Figure 15, most DFPT-end-capped thin films (50 nm) show lower LUMO/HOMO energies as measured by UPS, compared to the electrochemically derived energy levels. For example, the electrochemically derived LUMO/HOMO energy levels for

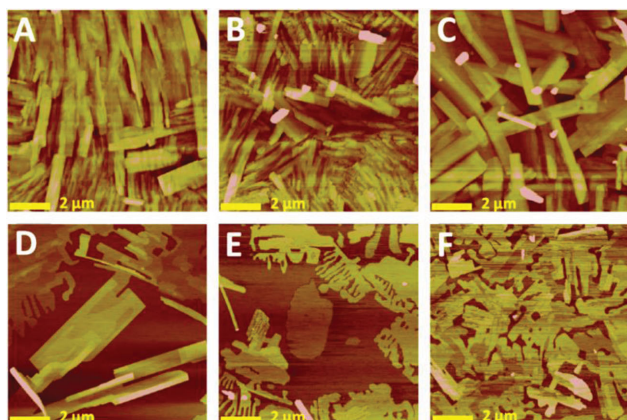


**Figure 13.** Comparison of bulk film and submonolayer film morphology of DFPT-DTT (AFM images): A) 50 nm, on bare SiO<sub>2</sub>, B) 50 nm, on HMDS-treated Si/SiO<sub>2</sub>, C) 50 nm, on OTS-treated Si/SiO<sub>2</sub>, D) 3 nm, on bare SiO<sub>2</sub>, E) 3 nm, on HMDS-treated Si/SiO<sub>2</sub>, and F) 3 nm, OTS-treated Si/SiO<sub>2</sub>. All films were grown at  $T_D = 110^\circ\text{C}$  ( $10\ \mu\text{m} \times 10\ \mu\text{m}$ ).

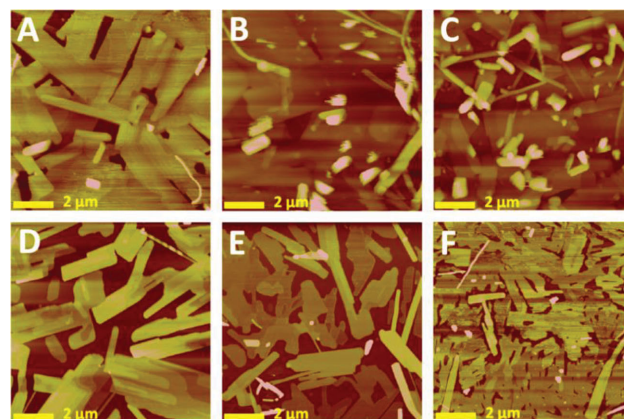


**Figure 14.** Comparison of bulk film and submonolayer film morphology of DFPT-TT (AFM images): A) 50 nm, on bare SiO<sub>2</sub>, B) 50 nm, on HMDS-treated Si/SiO<sub>2</sub>, C) 50 nm, on OTS-treated Si/SiO<sub>2</sub>, D) 3 nm, on bare SiO<sub>2</sub>, E) 3 nm, on HMDS-treated Si/SiO<sub>2</sub>, and F) 3 nm, OTS-treated Si/SiO<sub>2</sub>. All films were grown at  $T_D = 110^\circ\text{C}$  ( $10\ \mu\text{m} \times 10\ \mu\text{m}$ ).

DFPT-TTA are  $-2.57/-5.31\ \text{eV}$ , while those of DFPT-TTA thin films are  $-2.44/-4.95\ \text{eV}$  on bare Si and  $-3.06/-5.57\ \text{eV}$  on OTS-treated substrates, respectively (Figure 15). Similar trends are observed for both DFPT-DTT and DFPT-TT films (Figure 15). The difference in energy levels between solution measurements and thin films is likely due to the structures of the condensed films, solvation effects, and/or experimental conditions, although direct correlations of energy levels obtained by different experimental techniques are known to be imprecise.<sup>[57–59]</sup> Comparing thin film energy levels on different substrates, all of the DFPT-end-capped thin films on OTS-treated substrates exhibit lower LUMO/HOMO energies versus those on bare Si (Figure 15). LUMO/HOMO energy differences on OTS-treated and bare Si substrates are 0.62 eV for DFPT-TTA thin films, larger than those for DFPT-DTT (0.23 eV) and DFPT-TT (0.27 eV) thin films. Lower LUMO energies on OTS-treated substrates are likely to decrease electron injection barriers, affording enhanced device performance (vide supra).<sup>[56]</sup>

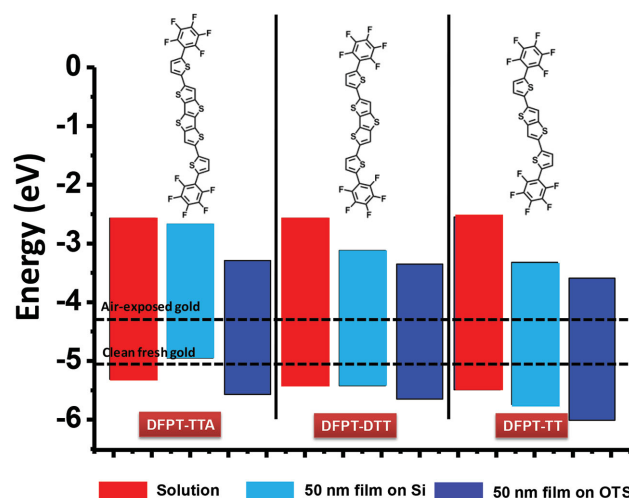


**Figure 15.** HOMO–LUMO energy diagram of DFPT-TTA ( $T_D = 110^\circ\text{C}$ ), DFPT-DTT ( $T_D = 25^\circ\text{C}$ ), and DFPT-TT ( $T_D = 25^\circ\text{C}$ ) thin films on Si and on OTS-treated Si substrates, as characterized by ultraviolet photoelectron spectroscopy.

### 3. Conclusions

We demonstrated here that extending the  $\pi$ -conjugated backbone is an effective molecular design approach to optimize n-type organic semiconductors composed of perfluorinated fused thiophenes. Additionally, two thiophenes incorporated in the fused thiophene backbones yield n-type organic semiconductors, with mobilities approaching  $0.43 \text{ cm}^2 \text{ V}^{-1} \text{ s}^{-1}$ . Thin films of DFPT-TTA, DFP-TTA, and DFP-DTT exhibit a hypsochromic optical absorption shift, while those of DFPT-DTT and DFPT-TT exhibit bathochromic shifts. In addition, substrate OTS treatment not only enhances the growth of contiguous charge transport pathways within the first few monolayers of the semiconductor film by enhancing film structural quality on the dielectric surface, but also decreases electron injection barriers by lowering the LUMO energy. We believe that our study on new DFPT molecules can suggest a benchmark example to guide developing new generations of high-performance organic semiconductors based on fused thiophenes in the future.

### 4. Experimental Section

**Materials and Methods:** All chemicals and solvents were of reagent grade and were obtained from Aldrich, Arco, or TCI Chemical Co. Solvents for reactions (toluene, benzene, ether, and THF) were distilled under  $\text{N}_2$  from sodium/benzophenone ketyl, and halogenated solvents were distilled from  $\text{CaH}_2$ .  $^1\text{H}$  and  $^{13}\text{C}$  NMR spectra were recorded on Bruker 500, 300, or DRX-200 instruments. Chemical shifts for  $^1\text{H}$  and  $^{13}\text{C}$  spectra were referenced to solvent peaks.  $^{19}\text{F}$  NMR spectra were referenced to external  $\text{CFCl}_3$ . DSC was carried out on a Mettler DSC 822 instrument, and calibrated with a pure indium sample at a scan rate of  $10 \text{ K min}^{-1}$ . Thermogravimetric analysis (TGA) was performed on a Perkin Elmer TGA-7 thermal analysis system using dry  $\text{N}_2$  as the carrier gas at a flow rate of  $40 \text{ mL min}^{-1}$ . The UV-vis absorption and fluorescence spectra were obtained using JASCO V-530 and Hitachi F-4500 spectrometers, respectively, and all spectra were measured in a specified solvent at room temperature. The IR spectra were obtained using a JASCO FT/IR-4100 spectrometer. Differential pulse voltammetry experiments were performed with a CH Instruments model CHI621C Electrochemical Analyzer. All measurements were carried out at a specified temperature with a conventional three-electrode configuration consisting of a Pt disk working electrode, an auxiliary Pt wire electrode, and a nonaqueous Ag reference electrode. The supporting electrolyte was  $0.1 \text{ M}$  tetrabutylammonium hexafluorophosphate ( $\text{TBAPF}_6$ ) in the dry solvent specified. All potentials reported here are referenced to an  $\text{Fc}^+/\text{Fc}$  internal standard (at  $+0.6 \text{ V}$ ). Elemental analyses were performed on a Heraeus CHN-O-Rapid elemental analyzer. Mass spectrometric data were obtained with a JMS-700 HRMS instrument. Prime grade silicon wafers ( $\text{p}^+-\text{Si}$ ) with  $\approx 300 \text{ nm}$  ( $\pm 5\%$ ) thermally grown oxide (Wafer Reclaim Service) were used as device substrates. The reagents 2-bromo-5-pentafluorophenylthiophene,<sup>[60]</sup> TT,<sup>[61]</sup> DTT,<sup>[62]</sup> and TTA<sup>[28]</sup> were prepared according to literature procedures.

**Synthesis of DFPT-TTA:** Under nitrogen at  $0^\circ\text{C}$ ,  $n\text{-BuLi}$  ( $2.5 \text{ M}$ ,  $0.8 \text{ mL}$  in hexanes,  $2.00 \text{ mmol}$ ) was added to a  $20 \text{ mL}$  THF solution of TTA ( $220 \text{ mg}$ ,  $0.87 \text{ mmol}$ ) and the mixture was stirred at this temperature for  $1 \text{ h}$ . Tris- $n$ -butylstannyl chloride ( $0.54 \text{ mL}$ ,  $2.00 \text{ mmol}$ ) in  $10 \text{ mL}$  THF was then added into the mixture and stirred for  $30 \text{ min}$  at  $0^\circ\text{C}$ . The mixture was then stirred at room temperature for  $12 \text{ h}$ . THF was next removed under vacuum and a  $10 \text{ mL}$  toluene solution of dry 2-bromo-5-pentafluorophenylthiophene ( $0.658 \text{ g}$ ,  $2.00 \text{ mmol}$ ) as well as a  $20 \text{ mL}$  toluene solution of tetrakis(triphenylphosphine)palladium ( $40 \text{ mg}$ ,  $0.03 \text{ mmol}$ ) were added and the mixture was refluxed for  $2 \text{ d}$ . Water was added to quench the reaction. The solid product was filtered and washed with hexane, and was further purified by gradient

sublimation at a pressure of  $<10^{-4}$  Torr, giving a bright yellow solid DFPT-TTA ( $913 \text{ mg}$ ) in a yield of  $61\%$ .  $M_p$ :  $329^\circ\text{C}$ .  $^1\text{H}$  NMR ( $500 \text{ MHz}$ ;  $\text{C}_2\text{D}_2\text{Cl}_4$ ): not sufficiently soluble to obtain a spectrum even at  $70^\circ\text{C}$ . Anal. calcd. for  $\text{C}_{30}\text{H}_6\text{F}_{10}\text{S}_6$ : C,  $48.12$ ; H,  $0.81$ ; found: C,  $48.47$ ; H,  $0.95$ ; MS (EI)  $m/z$  calcd. for  $\text{C}_{30}\text{H}_6\text{F}_{10}\text{S}_6$ :  $747.86$  ( $M^+$ ). Found:  $747.86$ . HRMS  $m/z$  calcd. for  $\text{C}_{30}\text{H}_6\text{F}_{10}\text{S}_6$ :  $747.8634$  ( $M^+$ ). Found:  $747.8629$ .

**Synthesis of DFPT-DTT and DFPT-TT:** DFPT-DTT and DFPT-TT were prepared via similar procedures except DTT or TT was used and THF was replaced with ether in the fused thiophene stannylation reaction. Further purification was done by gradient sublimation at a pressure of  $<10^{-4}$  Torr, giving a bright yellow solid DFPT-DTT in a yield of  $65\%$ .  $M_p$ :  $319^\circ\text{C}$ .  $^1\text{H}$  NMR ( $500 \text{ MHz}$ ;  $\text{C}_2\text{D}_2\text{Cl}_4$ ): not sufficiently soluble to obtain a spectrum even at  $70^\circ\text{C}$ . Anal. calcd. for  $\text{C}_{28}\text{H}_6\text{F}_{10}\text{S}_5$ : C,  $48.55$ ; H,  $0.87$ ; found: C,  $48.83$ ; H,  $0.98$ ; MS (EI)  $m/z$  calcd. for  $\text{C}_{28}\text{H}_6\text{F}_{10}\text{S}_5$ :  $691.89$  ( $M^+$ ). Found:  $691.89$ . HRMS  $m/z$  calcd. for  $\text{C}_{28}\text{H}_6\text{F}_{10}\text{S}_5$ :  $691.8913$  ( $M^+$ ). Found:  $691.8908$ . Similarly, DFPT-TT was obtained in a yield of  $55\%$ .  $M_p$ :  $239^\circ\text{C}$ .  $^1\text{H}$  NMR ( $300 \text{ MHz}$ ,  $\text{CDCl}_3$ ):  $\delta$   $7.49$  (d,  $J = 3.6 \text{ Hz}$ ,  $2\text{H}$ ),  $7.41$  (s,  $2\text{H}$ ),  $7.33$  (d,  $J = 3.6 \text{ Hz}$ ,  $2\text{H}$ ).  $^{19}\text{F}$  NMR ( $282 \text{ MHz}$ ,  $\text{CDCl}_3$ ):  $\delta$   $-139$ ,  $-155$ ,  $-161$ .  $^{13}\text{C}$  NMR ( $125 \text{ MHz}$ ;  $\text{C}_2\text{D}_2\text{Cl}_4$ ): not sufficiently soluble. Anal. calcd. for  $\text{C}_{26}\text{H}_6\text{F}_{10}\text{S}_4$ : C,  $49.06$ ; H,  $0.95$ ; found: C,  $49.13$ ; H,  $1.02$ ; MS (EI)  $m/z$  calcd. for  $\text{C}_{26}\text{H}_6\text{F}_{10}\text{S}_4$ :  $635.91$  ( $M^+$ ). Found:  $635.91$ . HRMS  $m/z$  calcd. for  $\text{C}_{26}\text{H}_6\text{F}_{10}\text{S}_4$ :  $635.9193$  ( $M^+$ ). Found:  $635.9185$ .

**Single Crystal Structure Determination of DFPT-TTA, DFPT-DTT, and DFPT-TT:** Crystals suitable for X-ray diffraction were obtained from a hot 1,2,4-trichlorobenzene solutions of DFPT-TTA, DFPT-DTT, and DFPT-TT. A light green plate crystal of DFPT-TTA having approximate dimensions of  $0.41 \times 0.13 \times 0.02 \text{ mm}$  was mounted using oil (Infinitec V8512) on a glass fiber. The single crystal of DFPT-DTT had an orange color with dimensions of  $0.28 \times 0.16 \times 0.08 \text{ mm}$ . Orange needle-like crystals of DFPT-TT for X-ray diffraction were obtained from a hot solution of toluene with dimensions of  $0.59 \times 0.15 \times 0.04 \text{ mm}$ . All measurements were made on a Bruker APEX-II CCD detector with graphite monochromated  $\text{Cu K}\alpha$  radiation at  $100(2) \text{ K}$ . After data collection, the frames were integrated and absorption corrections were applied. The initial crystal structure was solved by direct methods, the structure solution was expanded through successive least-squares cycles, and the final solution was determined. All of the nonhydrogen atoms were refined anisotropically. Hydrogen atoms attached to carbon atoms were fixed at calculated positions and refined using a riding mode. Crystal data and refinement parameters are summarized in Tables S1–S3 (Supporting Information).

**Thin Film Characterization: Grazing Incidence X-ray Diffraction (GIXRD):** GIXRD measurements were performed on a Rigaku ATX-G instrument. Samples were mounted in ambient on the stage of a three-axis goniometer. The sample surface was then irradiated by a monochromatic  $5.0 \times 0.1 \text{ mm}^2$  (horizontal  $\times$  vertical) X-ray beam at an incident angle of  $0.4^\circ$ . The data are plotted as a function of vector is defined as  $q = [4\pi \sin(\theta/2)/\lambda]$ , where  $\theta$  and  $\lambda$  are the angle and wavelength of the X-ray ( $\text{Cu K}\alpha$ ,  $\lambda = 0.154 \text{ nm}$ ).

**Grazing Incidence Wide Angle X-ray Scattering: GIWAXS:** Measurements were performed at Beamline 33-BM of the Advanced Photon Source (APS) at Argonne National Laboratory. Scattering intensities are expressed as a function of the scattering vector,  $q = 4\pi \sin(\theta)/\lambda$ , where  $\theta$  is the half scattering angle and  $\lambda = 1.6868 \text{ \AA}$  is the wavelength of incident radiation. An area detector situated  $200.4 \text{ mm}$  from the sample was used to collect the scattered X-rays. The incident angle was  $0.12^\circ$ .

**UV Absorption Measurements:** Thin films were deposited on quartz glass and optical absorption was measured by Varian Cary 5000 spectrophotometer.

**OTFT Fabrication:** Thin film transistors were fabricated in a bottom gate-top contact configuration. Highly doped p-type (100) silicon wafers ( $<0.004 \Omega \text{ cm}$ ) were used as gate electrodes as well as substrates, and  $300 \text{ nm SiO}_2$  thermally grown on Si was used as the gate insulator. The unit area capacitance is  $11.4 \text{ nF cm}^{-2}$ . The substrate surface was treated with n-OTS and HMDS purchased from Sigma-Aldrich Chemical Co. For HMDS treatment, a few drops of HMDS were loaded inside a self-assembly chamber under an  $\text{N}_2$  blanket. The  $\text{SiO}_2/\text{Si}$  substrates were exposed to this atmosphere for at least  $7 \text{ d}$  to give a hydrophobic surface. After HMDS deposition, the advancing aqueous contact angle

was 95°. For OTS treatment, OTS was deposited in  $3 \times 10^{-3}$  M hexane solution in air after 10 h of solution aging under 55%–60% of relative humidity. Then the substrate was sonicated with hexane, acetone, and ethanol in sequence. After finishing OTS treatment, the advancing aqueous contact angle of a water drop was 104°. Semiconductor thin films (50 nm) were next vapor-deposited onto the substrates held at predetermined temperatures of 25, 80, 110 °C with a deposition rate of  $0.1 \text{ \AA s}^{-1}$  at  $6 \times 10^{-6}$  Torr, employing a high-vacuum deposition chamber (Denton Vacuum, Inc., USA). Gold source and drain electrodes (50 nm) were vapor-deposited at  $2 \times 10^{-6}$  Torr through a shadow mask in the vacuum deposition chamber. Devices were fabricated with a typical channel length of 100  $\mu\text{m}$ , and a channel width of 5000  $\mu\text{m}$ .

**OTFT Characterization:**  $I$ – $V$  plots of device performance were measured under vacuum and in air, and transfer and output plots were recorded for each device. The  $I$ – $V$  characteristics of the devices were measured using a Keithley 6430 subfemtoammeter and a Keithley 2400 source meter, operated by a local Labview program and GPIB communication. Key device parameters, such as charge carrier mobility ( $\mu$ ), threshold voltage ( $V_T$ ), and on-to-off current ratio ( $I_{on}/I_{off}$ ), were extracted from the source–drain current ( $I_{SD}$ ) versus source–gate voltage ( $V_{SG}$ ) characteristics employing standard procedures.<sup>[47]</sup> Mobilities were obtained from the formula defined by the saturation regime in transfer plots,  $\mu = 2I_{SD}L/[C_iW(V_{SG} - V_T)^2]$ , where  $I_{SD}$  is the source–drain current,  $V_{SG}$  is source–gate voltage,  $V_T$  is the threshold voltage. Threshold voltage was obtained from  $x$  intercept of  $V_{SG}$  versus  $I_{SD}^{1/2}$  plots.

**Film Morphology Measurements:** AFM measurements were performed by using a JEOL-Microscope (JEOL Ltd. Japan) and a Dimension Icon Scanning Probe Microscope (Veeco, USA) in a tapping mode.

## Supporting Information

Supporting Information is available from the Wiley Online Library or from the author.

## Acknowledgements

J.Y. and S.V. contributed equally to this work. This research was supported by the NSF MRSEC program (Grant No. DMR-1121262) at the Materials Research Center of Northwestern U., by AFOSR Grant No. FA9550-08-1-0331, by the National Science Council, Taiwan, Republic of China (Grant Nos. NSC102-2923-M-008-004-MY2 and MOST 103-2113-M-008-004), and by Basic Science Research Program through the National Research Foundation of Korea (NRF) funded by the Ministry of Science, ICT and Future Planning (NRF-2014R1A1A1A05002158) and by the Center for Advanced Soft Electronics under the Global Frontier Research Program of the Ministry of Science, ICT and Future Planning (Code No. 2013M3A6A5073175). Use of the Advanced Photon Source, 33BM-C, was supported by the U.S. DOE, Office of Science, Office of Basic Energy Sciences, under Contract No. DE-AC02-06CH11357. This work made use of the J. B. Cohen X-ray Diffraction Facility.

Received: March 15, 2015

Revised: May 24, 2015

Published online: June 22, 2015

- [1] a) H. Yan, Z. H. Chen, Y. Zheng, C. Newman, J. R. Quinn, F. Dotz, M. Kastler, A. Facchetti, *Nature* **2009**, 457, 679; b) C. Kim, A. Facchetti, T. J. Marks, *Science* **2007**, 318, 76; c) B. A. Jones, A. Facchetti, M. R. Wasielewski, T. J. Marks, *J. Am. Chem. Soc.* **2007**, 129, 15259; d) H. Usta, C. Kim, Z. Wang, S. Lu, H. Huang, A. Facchetti, T. J. Marks, *J. Mater. Chem.* **2012**, 22, 4459; e) H. Usta, M. D. Yilmaz, A.-J. Avestro, D. Boudinet, M. Denti, W. Zhao, J. F. Stoddart, A. Facchetti, *Adv. Mater.* **2013**, 25, 4327.

- [2] a) O. Knopfmacher, M. L. Hammock, A. L. Appleton, G. Schwartz, J. Mei, T. Lei, J. Pei, Z. Bao, *Nat. Commun.* **2014**, 5, 2954; b) Y. Diao, B. C.-K. Tee, G. Giri, J. Xu, D. H. Kim, H. A. Becerril, R. M. Stoltenberg, T. H. Lee, G. Xue, S. C. B. Mannsfeld, Z. Bao, *Nat. Mater.* **2013**, 12, 665; c) M. L. Tang, S. C. B. Mannsfeld, Y. S. Sun, H. A. Becerril, Z. Bao, *J. Am. Chem. Soc.* **2009**, 131, 882.
- [3] G. Yang, C. A. Di, G. Zhang, J. Zhang, J. Xiang, D. Zhang, D. Zhu, *Adv. Funct. Mater.* **2013**, 23, 1671.
- [4] a) W. Yue, T. He, M. Stolte, M. Gsanger, F. Würthner, *Chem. Commun.* **2014**, 50, 545; b) T. He, M. Stolte, F. Würthner, *Adv. Mater.* **2013**, 25, 6951.
- [5] a) P. J. Diemer, C. R. Lyle, Y. Mei, C. Sutton, M. M. Payne, J. E. Anthony, V. Coropceanu, J.-L. Bredas, O. D. Jurchescu, *Adv. Mater.* **2013**, 25, 6956; b) N. Shin, J. Kang, L. J. Richter, V. M. Prabhu, R. J. Kline, D. A. Fischer, D. M. Delongchamp, M. F. Toney, S. K. Satija, D. J. Gundlach, B. Purushothaman, J. E. Anthony, D. Y. Yoon, *Adv. Funct. Mater.* **2013**, 23, 366; c) S. Subramanian, S. K. Park, S. R. Parkin, V. Podzorov, T. N. Jackson, J. E. Anthony, *J. Am. Chem. Soc.* **2008**, 130, 2706; d) J. E. Anthony, *Chem. Rev.* **2006**, 106, 5028.
- [6] a) S. J. Noever, S. Fischer, B. Nickel, *Adv. Mater.* **2013**, 25, 2147; b) A. Avendano-Bolivar, T. Ware, D. Arreaga-Salas, D. Simon, W. Voit, *Adv. Mater.* **2013**, 25, 3095; c) Y. Didani, G. H. Mehl, A. Kumagai, N. Yoshimoto, C. Videlot-Ackermann, H. Brisset, *J. Am. Chem. Soc.* **2008**, 130, 17681.
- [7] a) Y. Zhao, Y. Guo, Y. Liu, *Adv. Mater.* **2013**, 25, 5372; b) L. Zhang, H. Wang, Y. Zhao, Y. Guo, W. Hu, G. Yu, Y. Liu, *Adv. Mater.* **2013**, 25, 5455.
- [8] K. Schmoltner, J. Kofler, A. Klug, E. J. W. List-Kratochvil, *Adv. Mater.* **2013**, 25, 6895.
- [9] a) T.-D. Tsai, J.-W. Chang, T.-C. Wen, T.-F. Guo, *Adv. Funct. Mater.* **2013**, 23, 4206; b) D. Khim, H. Han, K.-J. Baeg, J. Kim, S.-W. Kwak, D.-Y. Kim, Y.-Y. Noh, *Adv. Mater.* **2013**, 25, 4302.
- [10] a) D. Shukla, S. F. Nelson, D. C. Freeman, M. Rajeswaran, W. G. Ahearn, D. M. Meyer, J. T. Carey, *Chem. Mater.* **2008**, 20, 7486; b) F. Zhang, Y. Hu, T. Schuettfort, C.-A. Di, X. Gao, C. R. McNeill, L. Thomsen, S. C. B. Mannsfeld, W. Yuan, H. Sirringhaus, D. Zhu, *J. Am. Chem. Soc.* **2013**, 135, 2338; c) D. Liu, Z. He, Y. Su, Y. Diao, S. C. B. Mannsfeld, Z. Bao, J. Xu, Q. Miao, *Adv. Mater.* **2014**, 26, 7190; d) T. He, M. Stolte, C. Burschka, N. H. Hansen, T. Musiol, D. Käblein, J. Pflaum, X. Tao, J. Brill, F. Würthner, *Nat. Commun.* **2015**, 6, 5954.
- [11] a) Y. Mei, M. A. Loth, M. Payne, W. Zhang, J. Smith, C. S. Day, S. R. Parkin, M. Heeney, I. McCulloch, T. D. Anthopoulos, J. E. Anthony, O. D. Jurchescu, *Adv. Mater.* **2013**, 25, 4352; b) Y. Liu, Y. Wang, W. P. Wu, Y. Q. Liu, H. X. Xi, L. M. Wang, W. F. Qiu, K. Lu, C. Y. Du, G. Yu, *Adv. Funct. Mater.* **2009**, 19, 772.
- [12] X. Gao, Y. Hu, *J. Mater. Chem. C* **2014**, 2, 3099.
- [13] a) H. H. Fong, V. A. Pozdin, A. Amassian, G. G. Malliaras, D. M. Smilgies, M. Q. He, S. Gasper, F. Zhang, M. Sorensen, *J. Am. Chem. Soc.* **2008**, 130, 13202; b) F. Zhang, Y. Hu, T. Schuettfort, C.-A. Di, X. Gao, C. R. McNeill, L. Thomsen, S. C. B. Mannsfeld, W. Yuan, H. Sirringhaus, D. Zhu, *J. Am. Chem. Soc.* **2013**, 135, 2338.
- [14] a) C. Kim, P.-Y. Huang, J.-W. Jhuang, M.-C. Chen, J.-C. Ho, T.-S. Hu, J.-Y. Yan, L.-H. Chen, G.-H. Lee, A. Facchetti, T. J. Marks, *Org. Electron.* **2010**, 11, 1363; b) M. C. Chen, C. Kim, S. Y. Chen, Y. J. Chiang, M. C. Chung, A. Facchetti, T. J. Marks, *J. Mater. Chem.* **2008**, 18, 1029.
- [15] Y. N. Li, Y. L. Wu, P. Liu, Z. Prostran, S. Gardner, B. S. Ong, *Chem. Mater.* **2007**, 19, 418.
- [16] J. Kim, A. R. Han, J. H. Seo, J. H. Oh, C. Yang, *Chem. Mater.* **2012**, 24, 3464.
- [17] a) S. Nam, J. Jang, J. E. Anthony, J. J. Park, C. E. Park, K. Kim, *ACS Appl. Mater. Interfaces* **2013**, 5, 2146; b) W. H. Lee, D. Kwak,

- J. E. Anthony, H. S. Lee, H. H. Choi, D. H. Kim, S. G. Lee, K. Cho, *Adv. Funct. Mater.* **2012**, *22*, 267; c) J. Jang, S. Nam, K. Im, J. Hur, S. N. Cha, J. Kim, H. B. Son, H. Suh, M. A. Loth, J. E. Anthony, *Adv. Funct. Mater.* **2012**, *22*, 1005.
- [18] F. Zhang, C. Melzer, A. Gassmann, H. von Seggern, T. Schwalm, C. Gawrisch, M. Rehahn, *Org. Electron.* **2013**, *14*, 888.
- [19] M. Akhtaruzzaman, N. Kamata, J. Nishida, S. Ando, H. Tada, M. Tomura, Y. Yamashita, *Chem. Commun.* **2005**, 3183.
- [20] a) P.-Y. Huang, L.-H. Chen, Y.-Y. Chen, W.-J. Chang, J.-J. Wang, K.-H. Lii, J.-Y. Yan, J.-C. Ho, C.-C. Lee, C. Kim, M.-C. Chen, *Chem. Eur. J.* **2013**, *19*, 3721; b) P.-Y. Huang, L.-H. Chen, C. Kim, H.-C. Chang, Y.-J. Liang, C.-Y. Feng, C.-M. Yeh, J.-C. Ho, C.-C. Lee, M.-C. Chen, *ACS Appl. Mater. Interfaces* **2012**, *4*, 6992; c) N. Zhou, K. Prabakaran, B. Lee, S. H. Chang, B. Harutyunyan, P. Guo, M. R. Butler, A. Timalina, M. J. Bedzyk, M. A. Ratner, S. Vegiraju, S. Yau, C.-G. Wu, R. P. H. Chang, A. Facchetti, M.-C. Chen, T. J. Marks, *J. Am. Chem. Soc.* **2015**, *137*, 4414.
- [21] a) C. Wang, Y. Zang, Y. Qin, Q. Zhang, Y. Sun, C.-A. Di, W. Xu, D. Zhu, *Chem. Eur. J.* **2014**, *20*, 13755; b) H. Zhong, J. Smith, S. Rossbause, A. J. P. White, T. D. Anthopoulos, M. Heeney, *Adv. Mater.* **2012**, *24*, 3205; c) C. Zheng, Y. Zang, E. Gann, C. R. McNeill, X. Zhu, C. A. Di, D. Zhu, *J. Am. Chem. Soc.* **2014**, *136*, 16176; d) J. Li, X. Qiao, Y. Xiong, H. Li, D. Zhu, *Chem. Mater.* **2014**, *26*, 5782; e) Q. Wu, S. Ren, M. Wang, X. Qiao, H. Li, X. Gao, X. Yang, D. Zhu, *Adv. Funct. Mater.* **2013**, *23*, 2277; f) S.-S. Cheng, P.-Y. Huang, M. Ramesh, H.-C. Chang, L.-M. Chen, C.-M. Yeh, C.-L. Fung, M.-C. Wu, C.-C. Liu, C. Kim, H.-C. Lin, M.-C. Chen, C.-W. Chu, *Adv. Funct. Mater.* **2014**, *24*, 2057.
- [22] a) H. Usta, W. C. Sheets, M. Denti, G. Generali, R. Capelli, S. Lu, X. Yu, M. Muccini, A. Facchetti, *Chem. Mater.* **2014**, *26*, 6542; b) W. Hong, C. Guo, B. Sun, Z. Yan, C. Huang, Y. Hu, Y. Zheng, A. Facchetti, Y. Li, *J. Mater. Chem. C* **2013**, *1*, 5624; c) M. Durso, D. Gentili, C. Bettini, A. Zanelli, M. Cavallini, F. D. Angelis, M. G. Lobello, V. Biondo, M. Muccini, R. Capelli, M. Melucci, *Chem. Commun.* **2013**, 49, 4298.
- [23] a) J. Youn, S. Kewalramani, J. D. Emery, Y. Shi, S. Zhang, H.-C. Chang, Y.-j. Liang, C.-M. Yeh, C.-Y. Feng, H. Huang, C. Stern, L.-H. Chen, J.-C. Ho, M.-C. Chen, M. J. Bedzyk, A. Facchetti, T. J. Marks, *Adv. Funct. Mater.* **2013**, *23*, 3850; b) M.-C. Chen, S. Vegiraju, C.-M. Huang, P.-Y. Huang, S. L. Yau, K. Prabakaran, W.-C. Chen, W.-T. Peng, I. Chao, C. Kim, Y.-T. Tao, *J. Mater. Chem. C* **2014**, *2*, 8892.
- [24] a) Y. M. Sun, Y. W. Ma, Y. Q. Liu, Y. Y. Lin, Z. Y. Wang, Y. Wang, C. G. Di, K. Xiao, X. M. Chen, W. F. Qiu, B. Zhang, G. Yu, W. P. Hu, D. B. Zhu, *Adv. Funct. Mater.* **2006**, *16*, 426; b) K. Xiao, Y. Liu, T. Qi, W. Zhang, F. Wang, J. Gao, W. Qiu, Y. Ma, G. Cui, S. Chen, X. Zhan, G. Yu, J. Qin, W. Hu, D. Zhu, *J. Am. Chem. Soc.* **2005**, *127*, 13281.
- [25] C. Kim, M.-C. Chen, Y. J. Chiang, Y. J. Guo, J. Youn, H. Huang, Y. J. Liang, Y. J. Lin, Y. W. Huang, T. S. Hu, G. H. Lee, A. Facchetti, T. J. Marks, *Org. Electron.* **2010**, *11*, 801.
- [26] M.-C. Chen, Y. J. Chiang, C. Kim, Y. J. Guo, S. Y. Chen, Y. J. Liang, Y. W. Huang, T. S. Hu, G. H. Lee, A. Facchetti, T. J. Marks, *Chem. Commun.* **2009**, 1846.
- [27] J. A. Letizia, A. Facchetti, C. L. Stern, M. A. Ratner, T. J. Marks, *J. Am. Chem. Soc.* **2005**, *127*, 13476.
- [28] J. Youn, P.-Y. Huang, Y.-W. Huang, M.-C. Chen, Y.-J. Lin, H. Hunag, R. P. Ortiz, C. L. Stern, M.-C. Chung, C.-Y. Feng, L.-H. Chen, A. Facchetti, T. J. Marks, *Adv. Funct. Mater.* **2012**, *22*, 48.
- [29] Measured with a Pt working electrode in an *o*-dichlorobenzene solution using 0.1 mol dm<sup>-3</sup> Bu<sub>4</sub>NPF<sub>6</sub> as the supporting electrolyte.
- [30] K. Lee, A. J. Heeger, *Synth. Met.* **2002**, *128*, 279.
- [31] R. Osterbacka, C. P. An, X. M. Jiang, Z. V. Vardeny, *Science* **2000**, *287*, 839.
- [32] H. Sirringhaus, P. J. Brown, R. H. Friend, M. M. Nielsen, K. Bechgaard, B. M. W. Langeveld-Voss, A. J. H. Spiering, R. A. J. Janssen, E. W. Meijer, P. Herwig, D. M. de Leeuw, *Nature* **1999**, *401*, 685.
- [33] D. Holmes, S. Kumaraswamy, A. J. Matzger, K. P. C. Vollhardt, *Chem. Eur. J.* **1999**, *5*, 3399.
- [34] M. D. Curtis, J. Cao, J. W. Kampf, *J. Am. Chem. Soc.* **2004**, *126*, 4318.
- [35] Compounds with different main core or side chains could exhibit totally different packing motifs/types. For example, different packing types for oligothiophenes and acenes with different main cores or side chains have been reported in the literatures. a) J. E. Anthony, *Chem. Rev.* **2006**, *106*, 5028; b) A. Facchetti, M.-H. Yoon, C. L. Stern, H. E. Katz, T. J. Marks, *Angew. Chem. Int. Ed.* **2003**, *42*, 3900; c) M.-H. Yoon, A. Facchetti, C. E. Stern, T. J. Marks, *J. Am. Chem. Soc.* **2006**, *128*, 5792.
- [36] a) R. J. Li, W. P. Hu, Y. Q. Liu, D. B. Zhu, *Acc. Chem. Res.* **2010**, *43*, 529; b) J. Rivnay, L. H. Jimison, J. E. Northrup, M. F. Toney, R. Noriega, S. F. Lu, T. J. Marks, A. Facchetti, A. Salleo, *Nat. Mater.* **2009**, *8*, 952.
- [37] H. Moon, R. Zeis, E. J. Borkent, C. Besnard, A. J. Lovinger, T. Siegrist, C. Kloc, Z. Bao, *J. Am. Chem. Soc.* **2004**, *126*, 15322.
- [38] G. Giri, E. Verploegen, S. C. B. Mannsfeld, S. Atahan-Evrenk, D. H. Kim, S. Y. Lee, H. A. Becerril, A. Aspuru-Guzik, M. F. Toney, Z. Bao, *Nature* **2011**, *480*, 504.
- [39] D. S. Chung, J. W. Park, J. H. Park, D. Moon, G. H. Kim, H. S. Lee, D. H. Lee, H. K. Shim, S. K. Kwon, C. E. Park, *J. Mater. Chem.* **2010**, *20*, 524.
- [40] A. L. Briseno, J. Aizenberg, Y. J. Han, R. A. Penkala, H. Moon, A. J. Lovinger, C. Kloc, Z. Bao, *J. Am. Chem. Soc.* **2005**, *127*, 12164.
- [41] H. Menzel, B. Weichart, A. Schmidt, S. Paul, W. Knoll, J. Stumpe, T. Fischer, *Langmuir* **1994**, *10*, 1926.
- [42] F. C. Spano, *Acc. Chem. Res.* **2010**, *43*, 429.
- [43] S. Paek, J. Lee, J. M. Ko, H. S. Lim, J. Lim, S. H. Cho, J. Y. Lee, C. Lee, *Mol. Cryst. Liq. Cryst.* **2009**, *504*, 52.
- [44] J. H. Choi, D. W. Cho, H. J. Park, S. H. Jin, S. Jung, M. Yi, C. K. Song, U. C. Yoon, *Synth. Met.* **2009**, *159*, 1589.
- [45] M. H. Yoon, A. Facchetti, C. E. Stern, T. J. Marks, *J. Am. Chem. Soc.* **2006**, *128*, 5792.
- [46] *Physical Chemistry*, 8th ed. (Eds: P. Atkins, J. de Paula), W. H. Freeman and Company, NY **2006**.
- [47] *Semiconductor Devices: Physics and Technology* (Ed: S. M. Sze), Wiley, NY **1985**.
- [48] Note that n-channel characteristics of compounds with relatively high LUMO energy level (as determined electrochemically) have been reported in the literature (e.g., ref. [28]). For thin films (in solid state), LUMO energy levels are lower than those in solution (Figure 15). Furthermore, depending on the nature of semiconductor–dielectric interface, band bending could occur, possibly affording electron injection.
- [49] a) M. Tello, M. Chiesa, C. M. Duffy, H. Sirringhaus, *Adv. Funct. Mater.* **2008**, *18*, 3907; b) G. Horowitz, *Adv. Funct. Mater.* **2003**, *13*, 53.
- [50] J. W. Orton, M. J. Powell, *Rep. Prog. Phys.* **1980**, *43*, 1263.
- [51] G. E. Pike, C. H. Seager, *J. Appl. Phys.* **1979**, *50*, 3414.
- [52] H. Okamoto, N. Kawasaki, Y. Kaji, Y. Kubozono, A. Fujiwara, M. Yamaji, *J. Am. Chem. Soc.* **2008**, *130*, 10470.
- [53] W. Chen, D. C. Qi, H. Huang, X. Y. Gao, A. T. S. Wee, *Adv. Funct. Mater.* **2011**, *21*, 410.
- [54] G. Heimel, I. Salzmann, S. Duhm, J. P. Rabe, N. Koch, *Adv. Funct. Mater.* **2009**, *19*, 3874.
- [55] S. Duhm, G. Heimel, I. Salzmann, H. Glowatzki, R. L. Johnson, A. Vollmer, J. P. Rabe, N. Koch, *Nat. Mater.* **2008**, *7*, 326.
- [56] a) S. Kobayashi, T. Nishikawa, T. Takenobu, S. Mori, T. Shimoda, T. Mitani, H. Shimotani, N. Yoshimoto, S. Ogawa, Y. Iwasa, *Nat.*

- Mater.* **2004**, *3*, 317; b) X. Lu, T. Minari, A. Kumatani, C. Liu, K. Tsukagoshi, *Appl. Phys. Lett.* **2011**, *98*, 243301.
- [57] C. Arantes, M. Scholz, R. Schmidt, V. Dehm, M. L. M. Rocco, A. Scholl, F. Reinert, F. Wurthner, *Appl. Phys. A* **2012**, *108*, 629.
- [58] B. W. D'Andrade, S. Datta, S. R. Forrest, P. Djurovich, E. Polikarpov, M. E. Thompson, *Org. Electron.* **2005**, *6*, 11.
- [59] P. Djurovich, E. I. Mayo, S. R. Forrest, M. E. Thompson, *Org. Electron.* **2009**, *10*, 515.
- [60] A. Facchetti, M. H. Yoon, C. L. Stern, H. E. Katz, T. J. Marks, *Angew. Chem. Int. Ed.* **2003**, *42*, 3900.
- [61] L. S. Fuller, B. Iddon, K. A. Smith, *J. Chem. Soc., Perkin Trans. 1* **1997**, 3465.
- [62] J. Frey, A. D. Bond, A. B. Holmes, *Chem. Commun.* **2002**, 2424.
-